The Pennsylvania State University

The Graduate School

College of Engineering

A Higher Order Vortex-Lattice Method with a Force-Free Wake

A Thesis in

Aerospace Engineering

by

Götz Bramesfeld

Submitted in Partial Fulfillment

of the Requirements

for the Degree of

Doctor of Philosophy

August 2006

The thesis of Götz Bramesfeld was reviewed and approved* by the following:

Mark D. Maughmer
Professor of Aerospace Engineering
Thesis Advisor
Chair of Committee

Barnes W. McCormick
Professor Emeritus of Aerospace Engineering

Kenneth S. Brentner
Associate Professor of Aerospace Engineering

Farhan Gandhi
Associate Professor of Aerospace Engineering

Andrew L. Belmonte
Associate Professor of Mathematics

George A. Lesieutre
Professor of Aerospace Engineering
Head of the Department of Aerospace Engineering

*Signatures are on file in the Graduate School.

Abstract

A higher-order, lifting-surface method is presented that uses elements with distributed vorticity. As a consequence, the newly developed method is highly accurate in force prediction and numerically extremely robust, even when using a relaxed wake model. The accurate prediction is accomplished using lower panel densities than other methods require. The numerical robustness is achieved without compromising the irrotationality assumption, unlike other potential flow methods do that use discrete vortices with solid core models in the wake.

The distributed vorticity element of the newly developed method consists of a vortex sheet that holds streamwise vorticity that varies linearly over the element span. Transverse vorticity is concentrated in two vortex filaments that are located along the leading and trailing edge of the element. Their spanwise circulation distributions vary in a parabolic fashion. The circulation of the leading and trailing edge filaments are equal in magnitude, but opposite in orientations. By introducing additional singularities along the edges of the distributed vorticity elements, any extreme velocities associated with the edge singularities of the vortex sheets are removed. The velocity induced by a distributed vorticity element is determined with an analytical expression.

One or several spanwise systems of distributed vorticity elements are used to model the lifting surface and the wake that is relaxed using a time-stepping method. There, the shed vorticity forms an essentially continuous vortex sheet. Thus, because of the elimination of point or line singularities, many of the numerical problems are avoided that are encountered with conventional

vortex-lattice and panel methods. In addition, the continuous vorticity distribution across the lifting surface yields an accurate load prediction that is relatively insensitive to panel density changes on the lifting surface and in the wake. Consequently, significantly fewer singularity elements are needed to achieve accuracies comparable to other potential flow methods.

The subsequent method is a relatively fast tool for determining the location of the free wake and its interaction with complex wing geometries, especially when accurate load predictions are required. The potential of the method is demonstrated with two sample applications. Especially in the case of the formation flight of two aircraft, the relaxed wake model yields performance results that differ to those that are obtained with a fixed wake model.

Table of Contents

List of Figures

Nomenclature

A, B, C = circulation coefficients

A = aspect ratio, b^2/S

b = wingspan

c = chord

c_{mac} = mean aerodynamic chord

C_{Di} = induced drag

C_L = lift coefficient

c_l = section lift coefficient

ΔC_P = differential pressure coefficient between upper and lower surface

e = span efficiency factor: $C_{Di\ elliptic}/C_{Di}$

$\underline{F}'$ = sectional force

Δi_{tip} = differential incidence angle of wingtips, equivalent to an aileron

   deflection

k = positive constant

M_∞ = free stream Mach number

m = number of elements along the chord

n = number of elements along halfspan

n = surface normal

V_∞ = free stream velocity

w = downwash

$\underline{w}_1$ = velocity induced by vortex filament with a parabolic circulation distribution

$\underline{w}_2$ = velocity induced by a semi-infinite vortex sheet with a linear vorticity distribution in spanwise direction

$\underline{w}_3$ = velocity induced by a distributed vorticity element

Δx_{wake} = streamwise step size in wake

x, y, z = local reference frame

x_0, y_0, z_0 = reference or control point of distributed vorticity element

Δy = lateral spacing between fuselage centerlines

α = angle of attack

ε = incidence angle of distributed vorticity element

Γ = circulation

γ = vorticity

η_i = distributed vorticity-element half-span

φ = sweep angle of distributed vorticity element

ν = dihedral angle of distributed vorticity element

$\Delta\theta$ = relative pitch attitude

ξ_i = distributed vorticity-element half-chord

ξ, η, ζ = local reference frame of distributed vorticity element

ψ = yaw angle of distributed vorticity element

Indices

ht = horizontal tail

r = wing root

t = wingtip

Trefftz = values in Trefftz plane

l.e. = leading edge

t.e. = trailing edge

0 = center of distributed vorticity element

1 = left edge of distributed vorticity element

2 = right edge of distributed vorticity element

Acknowledgement

1   Introduction

Lift produced by a wing requires a pressure difference between the upper and lower surfaces. For a wing of finite span, this pressure difference results in a flow around the tips and, subsequently, in a general spanwise flow. Figure 1 shows the paths of air-particles moving above and below a wing having a positive angle of attack. On the lower surface, particles are deflected towards the wingtip, whereas they are deflected away from it on the upper surface. At the trailing edge the difference in direction of the upper and lower surface-flows causes a sheet of vorticity to be shed into the wake, which rolls-up further downstream. Although the basic mechanisms have been known and described for almost a century,[1,2,3] the prediction of the wake and its consequences are of considerable interest and still pose quite a challenge in the design and analysis of aircraft.
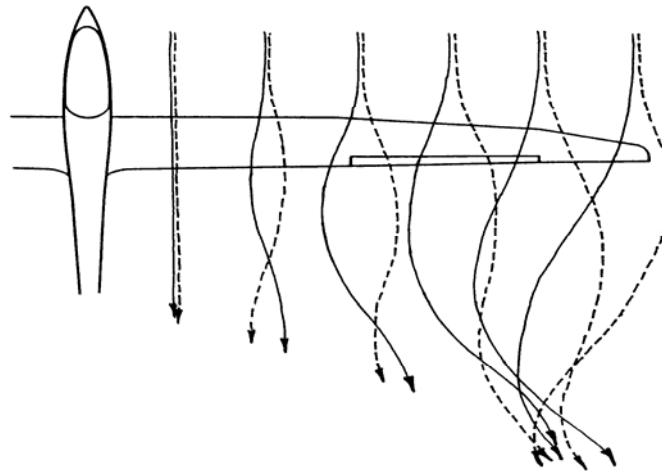
Figure 1: Streamlines over a wing at a positive angle of attack.[4]

1.1 Consequences from Lift and Wakes

The energy required to roll-up the wake is directly related to the induced drag of a wing. This effect is, to a large part, independent of viscosity, as can be seen in Fig. 2. In this figure the flow field behind the wing of an agricultural airplane is made visible with smoke. As the wake rolls up, the smoke particles move in concentric paths. With the exception of the very center of the rolled-up tip vortex, very little mixing occurs. This is a good indication that the shear forces are small and, consequently, that the flow is largely irrotational. The irrotational nature of the wake roll-up allows the application of potential flow theory for wake and induced drag investigations.

Figure 2: Rolled-up wake behind a crop duster.[5]

Induced drag accounts for about 80-percent of the total drag of transport aircraft during their critical climb out after take-off and for about 40-percent of their cruise drag.[6] Although the takeoff and climb out phase represent only a minor fraction of the overall operation of a transport aircraft, the large amount of

induced drag during this flight portion becomes a driving factor for sizing the wing area and the engine thrust. Thus, even a small reduction in induced drag can have major benefits for the overall performance of the aircraft.

In the case of high-performance sailplanes, the induced-to-total-drag ratio ranges from about 80-percent during high-angle of attack thermaling to about 20-percent during inter-thermal cruise.[7] Therefore, an induced drag reduction has the potential of increasing the average cross-country speeds with sailplanes. In recent decades, non-planar wing geometries, such as those with winglets and polyhedral planforms, have been relatively successful in enhancing fixed-wing aircraft performance by reducing their induced drags without excessively penalizing their parasite drags.

Much effort has also been invested into the investigation of the interaction between a lifting surface and its subsequent wake, such as is found with helicopter blades and wind-turbines. For example, when a helicopter blade passes through the wake of a proceeding one, highly unsteady aerodynamic effects result. These blade-wake interactions contribute significantly to the noise and the high vibratory loads of helicopters.[8] Structural vibrations mean significant wear to the engine, the transmission, and to the hub-blade assembly.

Another area where good wake prediction is beneficial is air-traffic control.[9] In order to avoid the upset of an aircraft from encountering the wake of a proceeding one, aircraft are currently separated rather conservatively by air-traffic control. In the worst case, loss of control and possible structural damage can be the result of such an encounter. The interest is to create a more flexible

and efficient separation practice so that the air-traffic capacity can be used more efficiently. A further interest is to tailor a lifting system in a way that its wake-vortex hazards are mitigated, which is especially a concern with the traffic separation that must follow very large commercial airliners.

1.2 A Brief Overview of Wing Analysis

According to the Kutta-Joukowsky theorem, when superimposing a circulation and a transverse flow in an ideal potential flow, a lift force is generated. For the case of wings with finite spans, Lanchester was the one to conceptually realize and describe that the bound circulation of such a wing cannot end at the wingtip, but results in a trailing vortex system downstream of the wing.[3] Essentially, the trailing system is required to satisfy Helmholtz theorem at the wingtips. This theorem states that a vortex cannot end or begin in the absence of rotationality. Lanchester also recognized that the work associated with the lift of a wing with a finite span is related to the kinetic energy of the flow field. Thus, the induced drag is the kinetic energy added to the wake per distanced traveled by the wing.

Prandtl expanded this model mathematically and his lifting-line theory became the first feasible tool for the analysis and design of wings of finite spans.[1,2] In this method, the wing is represented with a single bound vortex. As the strength of that bound vortex changes, vorticity is shed into the wake. In lifting-line theory, this shed vorticity is aligned with the free-stream and extends to infinity, resulting in a drag-free wake. Betz and Trefftz developed a method to determine the induced drag in the far field.[10,11] In the so called "Trefftz plane",

any influence of the bound circulation and the streamwise variation of shed vorticity have subsided. Thus, the problem is reduced to a two-dimensional one in the transverse plane. The subsequent induced drag depends solely on the shape and spanwise distribution of the circulation in the wake. This leads to Munk's "stagger theorem", which states that lifting systems with an identical spanwise distributions produce the same induced drag independently of the streamwise location of their bound circulations.[12] Thus, only the normal downwash of the trailing vortex system and the spanwise distribution of the bound circulation matter for drag purposes. The minimum induced drag of a planar wing planform is achieved with a wake having a uniform downwash distribution along the spanwise direction. Such a downwash field is produced by a wake with an elliptical spanwise circulation distribution.

Weissinger was able to extend the lifting-line theory to lifting surfaces with the introduction of collocation or control points.[13,14] By satisfying the flow-tangency condition in these locations, the strength of the bound circulation can be determined. Weissinger's approach has ultimately led to vortex-lattice and panel methods that use discrete vortex filaments or higher order panels.[15-17] These methods use systems of potential vortices, sources, and sinks, whose strengths are determined by satisfying the kinematic condition in control points that are distributed across the lifting surface. The linear nature of vortex-lattice and panel methods makes them ideal for the application for computers.

The fixed, drag-free wake models used by the classical lifting-line approach and the subsequent methods do not necessarily capture nonlinear

effects that are related to the rollup of the wake. Although the induced drag also depends on the shape of the wake, Prandtl reasoned that the wake rollup occurs relatively far downstream of wing, whereas the wake near the trailing edge, which has the greatest influence on the induced drag, is not deformed significantly. Thus for many applications, the drag-free wake model yields adequately accurate performance results. Nevertheless, the shape of a truly force-free wake is not only of interest for the improved performance predictions of planar and non-planar wing planforms, but also for other purposes, for example when several lifting surfaces have strong interactions.

Kaden studied the roll-up behavior of a zero-thickness vortex sheet in the Trefftz plane analytically.[18] Very soon after being released, the vortex sheet tends to roll-up to an almost axis-symmetric spiral with an infinite number of turns. This behavior is due to the infinitely large velocity gradients at the tip of the vortex sheet that has an elliptical circulation distribution in the spanwise direction. Although Krazny demonstrated that an infinitely thin free-wake sheet is numerically feasible with the help of smoothing parameters,[19] the numerical solution appears to be more robust when introducing thickness to the wake vortex-sheet.[20,21]

Modeling the relaxed wake with discrete vortex filaments can result in numerical issues due to the singular solution of the induced velocity in the center of a filament. Although a viscous-core model can eliminate any numerical erratic behavior in the wake,[22] it is in violation with the irrotationality assumption, one of the principles of the potential flow model. Besides the apparent confusion

between the mathematical model that is used to match the flow field and the actual flow field, the core size becomes a driving factor for the solution. Although the core size has only limited impact on the induced drag of a single wing, it may matter when the wake filaments of a wing pass in the proximity of the control points of another wing. Furthermore, issues like vortex pairing, the joining of two filaments in the wake that become close during the relaxation process, remain unresolved. Obviously, the solid core diameter would define the term "close" in that case.

The singularity issues of discrete vortex filaments can be avoided with distributed vorticity in the wake. Yeh developed a relaxed wake model that uses triangular elements with varying vorticity strengths.[23] The numerical application, however, has similar limitations as the discrete vortex model, primarily due to the singularities along the edges of the vortex sheets. Nagati uses smoothing functions instead of the singular velocities along the edges of the vortex-sheet elements of the relaxed wake model, which is essentially a "solid core" approach for distributed vorticity.[24]

1.3   Purpose of this Study

The modern tools for analyzing wakes have evolved quite impressively since the early days of induced drag estimation. In particular, the application of modern computers has yielded great gains. Despite the great advancements in computational speeds, better numerical tools are needed to improve wake-prediction methods that can be incorporated efficiently into the design process of

lifting surfaces or into the investigation of unsteady wake phenomena, such as of blade-vortex interaction.

The gains from a fast and precise analytical tool for dealing with the three-dimensional flow-field of a finite wing are substantial, such as significantly lower fuel consumption of transport aircraft, higher average cross-country speeds of gliders, reductions in helicopter vibrations and noise development, as well as more efficient and safer usage of the airways.

The development of a new theoretical prediction method of three-dimensional lift and the subsequent wake are described in this study. The method computes the lift distributions, wake shapes, and induced drag values with sufficient accuracy and speed such that it can be incorporated into the design process of fixed and rotary wings, including those having non-planar geometries. The computational solutions are achieved relatively fast and accurately by employing a refined theoretical model in combination with a simple numerical approach. Numerical accuracy and robustness of the method are achieved by using a relaxed, force free wake that is modeled as a vortex sheet.

In Chapter 2 a general overview is given about existing potential flow models. The newly developed method is introduced in Chapter 3. This includes the basic equations as well as a description of the modeling of the lifting surface and the wake. The validation of the method is discussed in Chapter 4, where the computational results are compared with the classical theory, other computational results, as well as experiments. Sample applications are introduced in Chapter 5 that demonstrate the potential of the method, in

particular its numerical robustness. A summary of the key results is listed in

Chapter 6.

2   Wings and Wakes

In the past, various methods have been developed to compute the three-dimensional flow-field around wings and their corresponding wake shapes. These methods differ in their prediction accuracy and in their computational speed, which are often conflicting qualities.

The following section describes how wings and their subsequent wakes can be modeled using a potential flow model. These models depend on the assumption of the flow being irrotationality and inviscid. The inviscid flow assumption is based on the observation that for a large part the flow field behind a wing displays very little viscous effects, as it is visible in Fig. 2. In this figure, the smoke particles on their concentric paths mix very little due to the absence of viscosity. The only exception is the relatively small core region of the tip vortex, where mixing occurs due to viscosity. Another region where viscosity is present is in the boundary layer near a surface. Outside of the viscous boundary layer, however, the flow can be considered to be irrotational.

2.1   Potential Flow

Potential-flow models generally provide relatively fast and accurate results, as long as the influence of any viscous effects, including flow separation, remains limited. These irrotational methods employ combinations of singularity elements, such as potential vortices, doublets, and sources, to model the desired flow field. Singularity elements superimpose a velocity field onto the free stream that decreases in strength with growing distance from the element. At the center,

the induced velocity often becomes infinite due to the singular nature of the element. An example of such a solution is a potential vortex with its concentric streamlines. The resulting circulation, Γ, remains constant as the tangential velocity decreases with growing distance to the vortex center. The circulation is defined as the line integral of the velocity, $\underline{V}$, around the closed curve, C:

$$\Gamma \equiv \oint_C \underline{V} \cdot d\underline{s} \qquad (1)$$

According to the Kutta-Joukowsky theorem, a potential vortex with the circulation $\underline{\Gamma}$ that is exposed to a free stream of velocity $\underline{u}$ and density ρ results in a sectional force:

$$\underline{F}' = \rho \underline{V}_\infty \times \underline{\Gamma} \qquad (2)$$

In the two-dimensional case of an infinite wing, the sectional lift is the product of the circulation, $\underline{\Gamma}$, density, ρ, and the free-stream with the velocity $\underline{V}_\infty$.

The mathematical solution with potential-flow elements is relatively trivial due to linear nature of their solutions. The linearity allows a simple superposition of several such elements in order to model even complicated geometries and flow problems. A vortex filament in the wake, however, creates a considerable challenge due to the infinitely large velocity at its center, which now bounds the region of interest. In order to avoid the numerical problems associated with these large velocities, a vortex core is sometimes modeled as a solid body with a finite radius that rotates in the viscous fluid at a constant angular velocity. In this case, the maximum tangential velocity occurs at the interface between the solid-body and the fluid. The rotationality is spread out over the finite solid core, as opposed to being confined to the infinitesimal vortex center.

11

2.2   Finite Wing Analysis

The lift produced by a wing can be modeled with a distribution of vorticity that is superimposed into the free-stream flow. Across the wing, the vorticity distribution and its magnitude are either pre-defined, or must satisfy certain boundary conditions. These boundary conditions are the flow-tangency requirement at the wing surface, the Kutta condition at the trailing edge, and an undisturbed free-stream flow at infinity. Very early on, Ref. 1 demonstrated that these boundary conditions lead to an equation with a double integral across the wing surface. Many potential flow methods use simplified vorticity-distribution models whose chordwise and/or spanwise vorticity is collapsed into discrete vortex filaments.

2.2.1   The Lifting-Line Model

The simplest lifting-line model, the horseshoe-vortex system, consists of the wing circulation lumped into a single potential vortex. As depicted in Fig. 3, the bound vortex is often assumed to be at the quarter-chord location, although it can be placed elsewhere, for example at the trailing edge.[25] Two trailing vortices coming off the wingtips and a starting vortex satisfy the second Helmholtz theorem, which states that an irrotational fluid cannot produce or dissipate vorticity. The starting vortex of the horseshoe-vortex system is considered to be located far downstream and, thus, not shown in this figure.
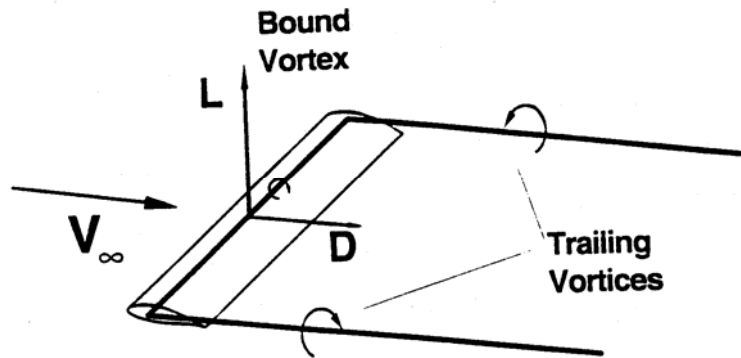
Figure 3: A horseshoe-vortex system.[7]

Instead of a single horseshoe vortex, the spanwise circulation variation may also be represented with several such systems that are distributed along the wingspan. The application of this lifting-line model satisfies the second Helmholtz theorem by shedding discrete trailing vortices that have the strength equal to that of the local change in bound vorticity. Taking the limit as the distance between the shed filaments goes to zero results in the trailing wake being modeled as a continuous vortex sheet. Whereas the velocities induced by a discrete trailing vortex filament become infinite as the singularity at the center of each filament is approached, the velocities induced by a vortex sheet remain finite with the exception of at the sheet itself, where the tangential velocity is singular. Therefore, the wake analysis is greatly simplified when the distributions of the bound vorticity and the subsequently shed vorticity can be described with a continuous function, for example, as that given by a Fourier series.[1,2,26,27] Although originally only used for straight wings, this theory has been extended for swept wings.[13,14]

The classical lifting-line method gives reasonably accurate predictions of the induced drag and lift-distributions of high-aspect ratio wings that are unswept and operating in symmetrical flow conditions.[26,27] It also predicts rolling moments reasonably well. A single lifting line, however, does not capture any chordwise information, such as the de-sweeping of the isobars at the center of a swept wing.[26,27]

More suitable for wings with sweep, low aspect ratios, or that are under asymmetrical flow conditions is the extended lifting-line method. This method uses control or collocation points where flow tangency is satisfied with an appropriate circulation distribution. These points are most commonly positioned at the three-quarter chord location, in order to produce the same pitching moment as a flat plate. This method is generally referred to as the Weissinger method.[13,14] This choice of the control-point locations, however, conflicts with the Kutta condition at the trailing edge. Nevertheless, the method computes reasonably good results for the spanwise lift distribution, the rolling moment, and the induced drag. To some extent, the method also provides pitching moments.[26,27]

2.2.2 The Lifting-Surface Model

The quality of the chordwise information can be improved with a multiple lifting-line method that uses several discrete lifting-lines that are distributed along the chord length.[28-30] The continuous distribution of the vorticity of the multiple lifting-lines in the chordwise direction leads to the lifting-surface method. This

14

classical approach of Ref. 1 and its double integral can be solved with a multi-parametric approach that describes the vorticity distribution.[31-34]

In general, lifting-surface methods provide accurate predictions for induced forces, as well as for the rolling and pitching moments. The quality of the estimated load distributions is quite reliable in both the spanwise and chordwise directions. A significant disadvantage is that the functions describing the vorticity distributions are rather complex. This is especially the case with discontinuous or non-planar wing geometries, such as present with flaps, multiple-lifting surfaces, or polyhedral planforms.[28]

More suited for the numerical investigation of complex geometries are vortex-lattice methods that divide a lifting surface into elementary wings in spanwise and chordwise direction. An example is shown in Fig. 4. Each elementary wing consists of a horseshoe vortex, whose bound vortex is placed along the quarter-chord location of the element. A control point is located at the three-quarter-chord point of the element midspan. Solving for flow tangency at the different control points leads to a system of linear equations whose solution yields the strength of each horseshoe vortex. The vortex-lattice method is capable of modeling relatively complicated geometries, including non-planar ones. Furthermore, it is computationally relatively efficient.
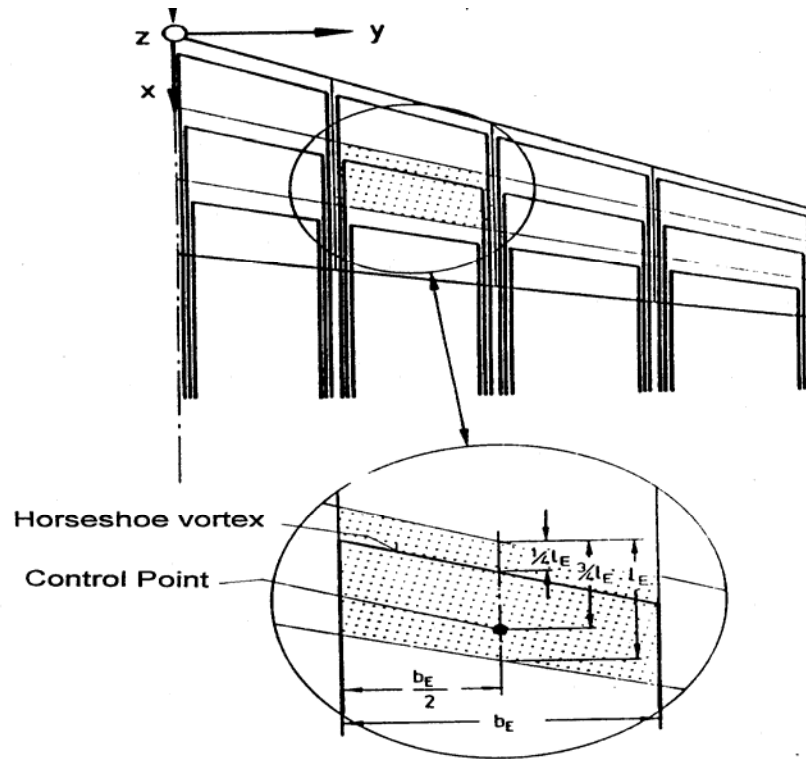
Figure 4: A vortex-lattice method with a system of horseshoe vortices.[28]

2.2.3 The Panel Method

Another class of methods that is well suited for the numerical analysis of planar and non-planar geometries is that of panel methods. They are, essentially, an extension of the vortex-lattice method through the introduction of thickness to the lifting surface.[15,16] The singularities that are used to satisfy the boundary conditions are arranged on the wing surface rather than along the mean chord, as is the case with vortex-lattice methods.

The quality of the numerical results for lift distributions and moments of planar as well as non-planar geometries for panel methods is similar to that of vortex-lattice methods. Despite the advances in computers, however, panel methods still require considerably more processing time than that required of

16

vortex-lattice methods. Thus, their application is often restricted to analysis

rather than design problems. Furthermore, panel codes have numerical

problems similar to those found with vortex-lattice methods that are due to the

singular nature of the trailing-vortex elements.

2.2.4   The Multiple Lifting-Line Method

Early lifting-line methods made use of circulation distributions described

by Fourier polynomials and whose shed wakes consist of continuous vortex

sheets.[1,2,14,26,27,31] In general, these methods are numerically well behaved and

do not have the same numerical problems as do distributions of discrete vortices.

A significant disadvantage is that the complexity of the function that describes the

bound-vorticity distribution increases substantially with the increasing complexity

of the lifting-surface geometry. Especially with geometric discontinuities, for

example due to flap deflections or winglets, it becomes difficult to find a function

that adequately describes the circulation distribution.

In order to be able to model more complex geometries, the multiple lifting

line method of Ref. 28 makes use of elementary wings that have a parabolic

circulation distribution in the spanwise direction, as shown in Fig. 5. The

magnitude and slope of the spanwise circulation distribution have to be

continuous across the common edge of two neighboring elements. The third

boundary condition for determining the exact parabolic shape is the flow-

tangency requirement at the control points. The result is a second-order spline

for the bound, spanwise circulation. Consequently, the shed vorticity is a sheet

with a continuous spanwise vorticity distribution that is a first-order spline. One

of the advantages of this method is that the induced velocities in the wake remain finite, even when approaching the sheet itself. In the plane of the sheet, the tangentially induced velocity is undetermined.

Because of the use of analytical solutions for computing the induced velocities, the multiple lifting-line method has proven to be fast and accurate enough to be employed in the design of complex wing geometries, such as wings with winglets.[35,36] A shortcoming of this method is its fixed wake model, which does not capture second-order effects that are due to the wake roll-up.
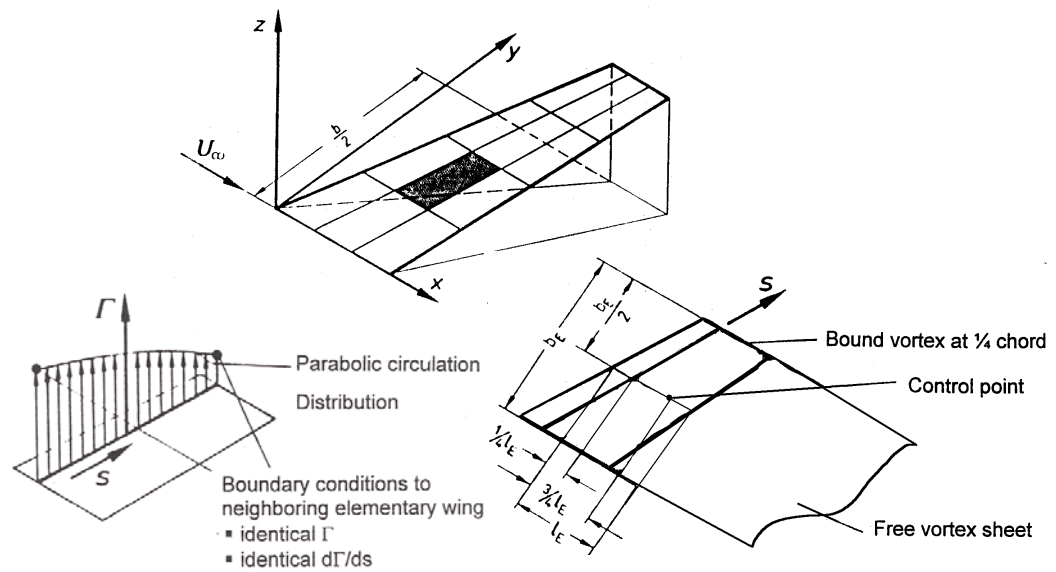
Figure 5: Wing paneling and elementary wings of the multiple lifting-line method.[28]

2.3   Wake Models

A free shear layer in the wake cannot support any forces after it has been shed from the trailing edge of a lifting surface. Thus, in order to remain free of any forces that are associated with the Kutta-Joukowsky theorem, the shed

18

vorticity is displaced by the local flow field. The velocities of the local flow field are induced by the lifting surface and the wake. The most evident result is the rollup of the vortex sheet soon after leaving the lifting surface. The behavior of the shed vorticity in the wake has a profound influence on the forces acting on the lifting surface due to the velocities that the wake induces.

2.3.1   Fixed Wakes

Three possible trajectories for the wake leaving the trailing edge of an airfoil are shown in Fig. 6. With a free-stream velocity parallel to the horizontal, wake *B*, which extends along the trailing-edge bisector, supports lift and drag loads that result from the induced velocities of the lifting surface and the wake itself. Additionally, the wake induces lift and drag forces onto the bound-vortex system. Although wake *B* probably models the flow conditions near the trailing edge quite realistically, further downstream the wake deviates considerably from the flow-field that is expected in reality. At sufficient distance downstream, the wake is most likely descending at a constant rate. With wake model *B*, the induced lift reduction is overestimated and the induced drag underestimated. Furthermore, the forces carried by the wake violate conservation of momentum.

Because it is aligned with the free stream, wake *A* is drag free. Despite that, the wake supports sideforces due to the velocities that the bound vortex and the wake itself induce. In the case of a simple horseshoe-vortex system, the two trailing vortex filaments carry the same magnitude in sideforce, although with opposite signs. Thus, at least in a global sense, the momentum of the wake is

conserved. Furthermore, forces that the wake induces onto the bound-vortex system are plane drag forces with no lift component.
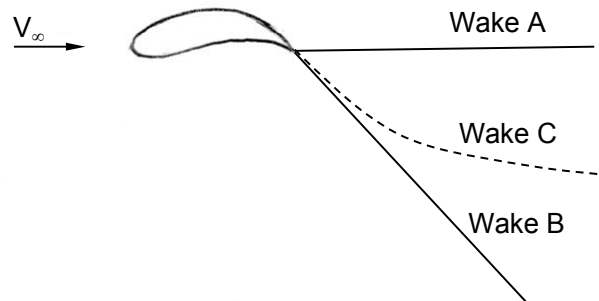
Figure 6: Possible wake shapes.[17]

The lesser computational effort of a fixed wake may justify the reduced accuracy of induced drag estimations. Although the fixed wake shape can be based on empirical results and may be of a non-straight shape similar to wake *C* in Fig. 6, the calculation of induced drag is greatly simplified in the Trefftz plane far downstream with a straight wake, such as wake *A*.[17,26,27] Furthermore, only the force-free wake that is aligned with the local velocities and the straight wake that is aligned with the free-stream ensure the conservation of the overall momentum of the wake at all angles of attack.

2.3.2 Free Wakes

A growing need exists for more accurate and faster wake-shape prediction tools, for example in order to investigate blade-vortex interactions of rotary-wing aircraft. A "true" wake cannot support any forces and, thus, has to be aligned with the local flow-field. The two most commonly used techniques for computing the free-wake shapes are spatial-relaxation and time-stepping methods.

The iterative spatial wake-relaxation method starts out with an assumed wake shape. The bound-vorticity strength and the velocity field in the wake are computed using this initial wake shape. In the next step, the wake-vortex filaments are displaced along the local flow direction in order to keep the wake force free. This process is repeated until a convergence criterion is satisfied.

In the time-stepping method, the flow-field and vorticity are iterated as the wing, which was previously at rest, starts moving instantaneously at the desired speed, V_∞. While the wing progresses, the wake evolves with each time step. Flow tangency is satisfied at the control points with a sufficient amount of circulation. The second Helmholtz theorem is satisfied with trailing vortex elements that are shed along the trailing-edge bisector. The length of these wake elements is the distance the wing progresses each time interval, $\Delta t \cdot V_\infty$. Based on the wake influence at each time step the wing circulation is adjusted so that the flow-tangency requirement is satisfied at the control points. The newly shed wake-vortex elements have the magnitude of the new bound-vortex circulation. After the new wake elements have been shed, the trailing vortex elements are aligned with the computed local flow-field.

The time-stepping method requires less wake computing steps than the spatial-relaxation method for the same flow-field size.[17] This is illustrated when considering n trailing vortices during k time steps. The time-stepping method requires $n \times k/2$ wake-velocity computations, whereas each iteration of the spatial relaxation method requires twice as many computations for a wake field of the same size.

2.4   Induced Forces

In addition to the free stream, the velocities that are induced onto a lifting surface by itself and its wake, result in forces. Mainly polyhedral or multiple wing geometries induce additional velocities parallel to the free stream that result in induced lift. This force is, however, relatively small when compared with the overall lift.

More complicated and of much greater interest is the determination of induced drag. Although generally somewhat larger in magnitude than induced lift, it is still relatively small. Furthermore, lift is fairly easily computed by applying the Kutta-Joukowsky theorem along the bound circulation using the free-stream velocity as well as any induced component that is parallel to the free stream. In the case of induced drag of a swept bound system, however, computing the velocity component that is induced at the bound vorticity and is normal to the free stream, becomes a function of the number of singularity elements used in the spanwise direction.[28,37] In the extreme, the velocity that a trailing continuous vortex sheet induces at its bound system is singular unless the bound circulation is unswept or remains constant in strength in spanwise direction.

If the bound system is swept, the velocity that a trailing system induces at the location of its bound-vortex system becomes singular. Despite the singular velocity solution, the induced drag of such a swept system remains finite and is equal to the value of an unswept system with the same spanwise circulation distribution.[12,37] For example, the drag of the unswept system A in Fig. 7 depends solely on the cross product of the bound circulations, Γ_i and Γ_{ii}, and the

velocities induced by their trailing systems. The bound vortices cannot induce

velocities onto each other, since their axes are in line. System B in that figure

represents a swept system that has been discretized. In this case, the bound

vortices do induce velocities onto each other that are proportional to $w_i \sim \Gamma_{ii}/d$

and $w_{ii} \sim \Gamma_i/d$ at bound vortices i and ii, respectively. The subsequent additional

drag forces that bound vortices i and ii produce are proportional to the cross

products of the induced velocity and the circulation, $D_i \sim w_i \Gamma_i \sim \Gamma_{ii}\Gamma_i/d$ and

$D_{ii} \sim w_{ii}\Gamma_{ii} \sim \Gamma_i\Gamma_{ii}/d$.[*] Even with different magnitudes of circulation i and ii, the

resulting forces are of the same magnitude. They are, however, of opposite

orientation and, thus, cancel, since bound vortex i induces velocities at bound

vortex ii that are coming out of the page, whereas bound vortex ii induces

velocities at bound vortex i that are into the page. Besides the additional drag

due to the velocities that the bound vortices induce on each other, another

change in the local induced drag of system B in Fig. 7 is due to the bound vortex

ii being an additional distance, d, further away from the influence of the trailing

system i. This reduction in drag, however, is compensated for by the additional

velocity induction at the other bound vortex i due to the additional length, d, of the

trailing system ii. Therefore, the overall induced drags of the vortex systems A

and B are equal despite the change in spanwise configuration. In contrast to

---

[*] To be more precise, the induced velocity has to be computed according to the Biot-
Savart law and requires the integration over the span of the bound vortex that induces the
velocity. The subsequent additional drag force is the result of the integral of the Kutta-Joukowsky
theorem over the span of the load-bearing vortex.

that, the computed induced drag of vortex system C in Fig. 7 yields a faulty result without any special consideration and separation of spanwise and streamwise vorticity of the swept bound-vortex systems. Thus, and in line with the stagger theorem,[12] it can be concluded that only the spanwise circulation, which is located on a plane perpendicular to the free stream, and the velocities induced by the streamwise vorticity affect induced drag.
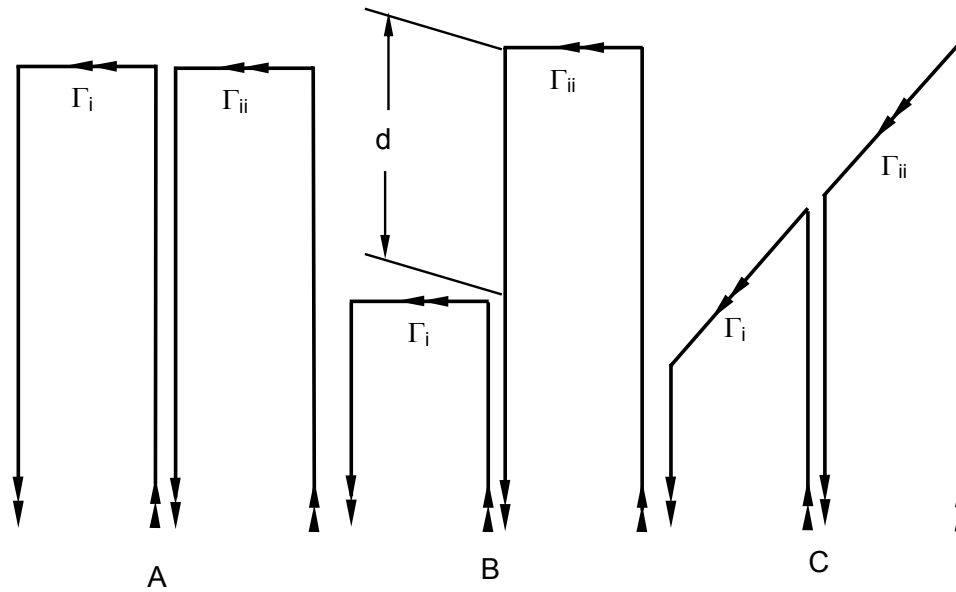
Figure 7: Three vortex systems that ultimately produce identical induced drag.

A convenient consequence of the stagger theorem allows the computation of the induced drag faraway downstream from the lifting surface in the Trefftz plane. The Trefftz plane, which is oriented perpendicular to the trailing vortex filaments, is sufficiently far downstream of the wing so that the velocities induced in the plane are unaffected by the bound vorticity and the wake shape has no streamwise variation.[10,11] In the Trefftz plane, the trailing vortices are of infinite length in either direction, compared to their semi-infinite nature in the vicinity of

the bound vorticity. Thus, the induced drag is easily computed by integrating the velocities of the, essentially, two-dimensional system within the Trefftz plane.

Many numerical methods compute induced drag by integrating the surface pressures at the lifting surface, with drag being the resulting force component that is parallel to the free-stream velocity. This approach exhibits less sensitivity to the exact shape of the rolled-up wake compared to the Trefftz-plane drag-calculation. The accuracy of the pressure integration, however, depends strongly on the numerical resolution, especially around the leading edge. Thus, the precision of this induced-drag prediction method is usually insufficient despite extensive computational efforts.[38-40]

Another method of induced-drag calculation recognizes that all of the vorticity that is produced by the lifting surface is shed into the wake at the trailing edge.[25, 38-40] This also happens to be the earliest location at which the wake-induced downward velocity is not blocked by the presence of the wing itself. Hence, the cross product of the lumped bound vorticity and the velocity that is induced along the trailing edge by the wake yields the induced drag.[25, 38-40] This drag-prediction method can be applied in vortex-lattice as well as panel codes. It has proven to be much more robust to small changes in the wake shape than, for example, is the case with Trefftz-plane drag calculations. It is also relatively insensitive to the paneling density of the lifting surface.[39-41]

2.5 Numerical Limitations of Discrete Singularity Solutions

Many limitations of the numerical methods used to analyze the finite wing problem are a consequence of the discrete nature of the singularities that are

25

used to model the flow field. One example is shown in Fig. 8 for the normalized

velocities that are induced by a continuous elliptical circulation distribution

compared to a model with ten discrete horseshoe vortices. The discretized

model is found to exhibit significant discretization errors, especially at the wingtip.

There, the induced velocity of the continuous circulation distribution remains

finite, while the one of the discretized model deviates significantly.

An increase in density of the horseshoe vortices only grants a limited

improvement in computational accuracy, but results in a considerable increase in

computational effort.[28] Additionally, reductions of the elementary-wing aspect-

ratio leads to growing numerical errors, as the influence of the trailing vortices on

the induced velocity at the control points increases disproportionally.
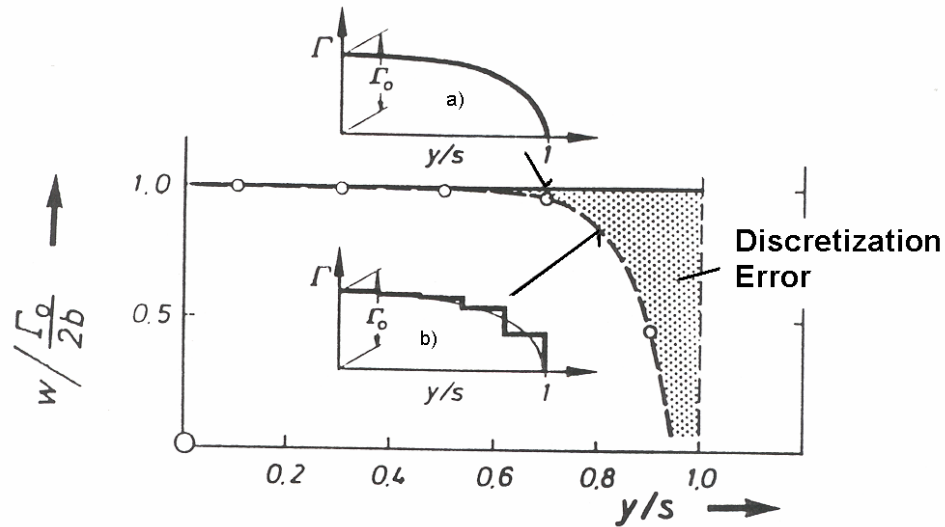
Figure 8: Error in induced velocity due to discretization of originally elliptical
circulation distribution.[28]

Other numerical problems are related to the large velocities that are

induced by the trailing vortices as they pass close by or through the control point

of another elementary wing. This problem mainly occurs during the modeling of

slipping flight conditions or with non-aligned horseshoe elements and relaxed wakes.[17.42]

Numerical problems also often arise during the relaxation process when a discretized potential flow model is used, as is the case for vortex filaments. In that particular example, the velocities that the filaments induce on one another can become very large or infinite, as their cores might get close during the relaxation process. One commonly employed solution is to use a solid core model around the core of wake filaments.[17] Although the solid core model appears to represent the viscous core of a vortex well, it is inconsistent with the irrotationality assumption on which the potential flow model and its singularity solutions are based. After all, the potential flow models are mathematical solutions for matching the boundary conditions of a specific flow field and not a representation thereof. In addition, the choice of the solid core size becomes the factor that drives the solution. One apparent limitation of such a model is the case when two solid cores become close during the relaxation process. It is unclear if the cores stay separate or join and, if they do join, what should the new solid core radius be.

3   A Lifting-Surface and Drag-Free Wake Model

A new potential flow method is introduced in this section. The method relies on distributed vorticity elements for modeling the lifting surface and the force free wake. Each element consists of a vortex filament along its leading and trailing edge. In addition, a vortex sheet in between ensures the continuity of the circulation. Using these distributed vorticity elements it is possible to model the wake as a continuous vortex sheet. As a consequence, the induced velocities in the wake are finite, avoiding many of the singularity problems of potential flow models that use line singularities in the wake, such as vortex filaments.   The subsequent wake-rollup behavior is numerically exceptionally robust.

3.1   Basic Equations

The lifting-surface method that is presented herein and its relaxed wake model are based on the multiple lifting-line method that is discussed in Chapter 2.2.4.[28] This particular lifting-line method uses one or several lifting lines that consist of several bound-vortex segments, so called elementary wings. As shown in Fig. 5, the bound-vortex segments are positioned along the quarter-chord line of the particular surface. The bound circulation of each elementary wing has a spanwise distribution of parabolic shape:

$$\Gamma(\eta) = A + \eta B + \eta^2 C \tag{3}$$

with η being the local span coordinate of that particular segment. The subsequent shed vortex sheet has a linear vorticity distribution in spanwise direction:

28

$$\gamma(\eta) \; = \; \frac{d\Gamma}{d\eta} = B + 2\eta C \tag{4}$$

Each shed wake is a semi-infinite vortex sheet that is aligned with the free stream and is, therefore, drag-free. Furthermore, it is noteworthy that circulation, Γ, and vorticity, γ, are vector quantities that are oriented in spanwise and streamwise direction, respectively.

The determination of the three circulation coefficients, A, B, and C, that describe the bound-circulation and shed-vorticity strength requires three boundary conditions. Similar to other panel or vortex-lattice methods, one of the boundary conditions is the flow tangency requirement at the control point that is located at the midspan of the ¾-chord line. The two remaining boundary conditions are given by the need of a continuous circulation and vorticity distribution across the boundary of two neighboring elementary wings.

In Ref. 28, analytical solutions are developed for the velocities that are induced by the bound vortex and its shed wake. The velocities that a vortex-filament segment induces with its parabolic circulation distribution at an arbitrary point, $P_0(\xi_0, \eta_0, \zeta_0)$, requires the integration over the elementary wingspan from $-\eta_i$ to η_i:

$$\underline{w}_1(\xi_0,\eta_0,\zeta_0) = \int_{-\eta_i}^{\eta_i} \frac{A+\eta B+\eta^2 C}{4\pi r_1^3} \begin{bmatrix} -\zeta_0 \\ \zeta_0\tan\varphi \\ \xi_0 - \eta_0\tan\varphi \end{bmatrix} d\eta \tag{5}$$

A similar integration yields the velocity that the semi-infinite vortex sheet induces:

$$\underline{w}_2\left(\xi_0,\eta_0,\zeta_0\right)=\int\limits_{-\eta_i}^{\eta_i}\frac{B+2\eta C}{4\pi\left(\left(\eta_0-\eta\right)^2+\zeta_0^2\right)^2}\left(\frac{\xi_0-\eta\tan\varphi}{r_1}+1\right)\begin{bmatrix}0\\-\zeta_0\\\eta_0-\eta\end{bmatrix}d\eta \qquad (6)$$

with

$$r_1=\sqrt{\left(\xi_0-\eta\tan\varphi\right)^2+\left(\eta_0-\eta\right)^2+\zeta_0^2}$$

ξ, η, and ζ are the coordinates in the local reference frame of the vortex filament and semi-infinite vortex sheet. The origin of the local reference frame is located at the midspan of the vortex filament and the ξ-axis points downstream along the centerline of the shed semi-infinite vortex sheet. The η-axis is in the spanwise direction of the local reference frame, which is a right-hand system. The bound vortex and the leading edge of the vortex sheet intersect the η-axis with the sweep angle, φ. The coefficients A, B, and C, describe the circulation and vorticity distribution in the spanwise direction, η, as used in Eqs. 3 and 4.

The analytical solutions of the integrals in Eqs. 5 and 6 are listed in Appendices 1 and 2, respectively. The solutions exhibit several singularities, the most obvious of which is at the center of the vortex filament. Other singularities are associated with the vortex sheet and require special attention. As is apparent in Eq. 6, the vortex sheet induces velocities that are normal to the plane of the sheet and tangential to it along the spanwise, η-, direction. Although the tangential velocity is singular in the plane of the vortex sheet, it remains finite up to the sheet. On either side of the vortex sheet, the tangentially induced velocities are of equal magnitudes, but opposite signs. In the plane of the sheet, the integral of Eq. 6 can be solved in the sense of the Cauchy-principal value.[37]

Additionally, the velocities that the vortex sheet induces normal to its plane-of-orientation are singular along the edges of the sheet. One such line of singular solutions is located along the leading edge of the semi-infinite vortex-sheet if it is swept. Without sweep, the self-induced velocity along the leading edge is half the value of what a double-infinite vortex sheet would induce. Further singularities are present along the side edges of the sheet. There, the normal velocity component is singular if the vorticity at the edge is non-zero.

In the case of a vortex sheet that has a continuous vorticity distribution, the normally induced velocity remains finite, even when modeling it using several sheet elements that have singularities along their sides. As long as the vorticity is continuous across the common boundary of two separate elements, the velocity singularities of the two neighboring vortex sheets are of equal magnitudes but opposite signs and, thus, cancel. In particular, the normal velocity that is induced by the linear spanwise vorticity distribution of a semi-infinite vortex sheet, depends, in part, on logarithmic terms of the following form:[28]

$$w_2(\eta_0) \sim \ln\left[\frac{(\eta_0 - \eta_i)^2}{(\eta_0 + \eta_i)^2}\right] \tag{7}$$

where η_0 is the local span coordinate of the point at which the induced velocity is computed, and η_i is the half span of the semi-infinite vortex-sheet element.

An example of the spanwise variation of the normal velocity that two semi-infinite vortex sheets induce in their plane some distance from their leading edges is shown in Fig. 9. Plotted are the normal velocities that each individual

vortex sheet induces, $w_{2\,left}$ and $w_{2\,right}$, as well as their combined normal velocity, $w_{2\,total}$. The "left" vortex sheet spans from $\eta = -1$ to 1. Its spanwise vorticity variation changes from $\gamma_{left} = 0$ to 3. The "right" vortex sheet is continuous with the latter vorticity value at $\eta = 1$. At its free end, $\eta = 4.2$, its vorticity becomes zero.

Although the individual velocities of each vortex sheet approach plus and minus infinity at their common boundary of $\eta = 1$, the total induced velocity, $w_{2\,total}$, remains finite since the singularities of $w_{2\,left}$ and $w_{2\,right}$ cancel. As the common boundary of the two neighboring elements is approached, the numerator of the logarithmic expression, as listed in Eq. 7, of one of the vortex-sheet elements becomes zero. Simultaneously, the denominator of the other element approaches zero as well. Consequently, since the logarithmic terms of are of equal size and opposite sign, the terms will cancel if the vorticities are of equal strength.
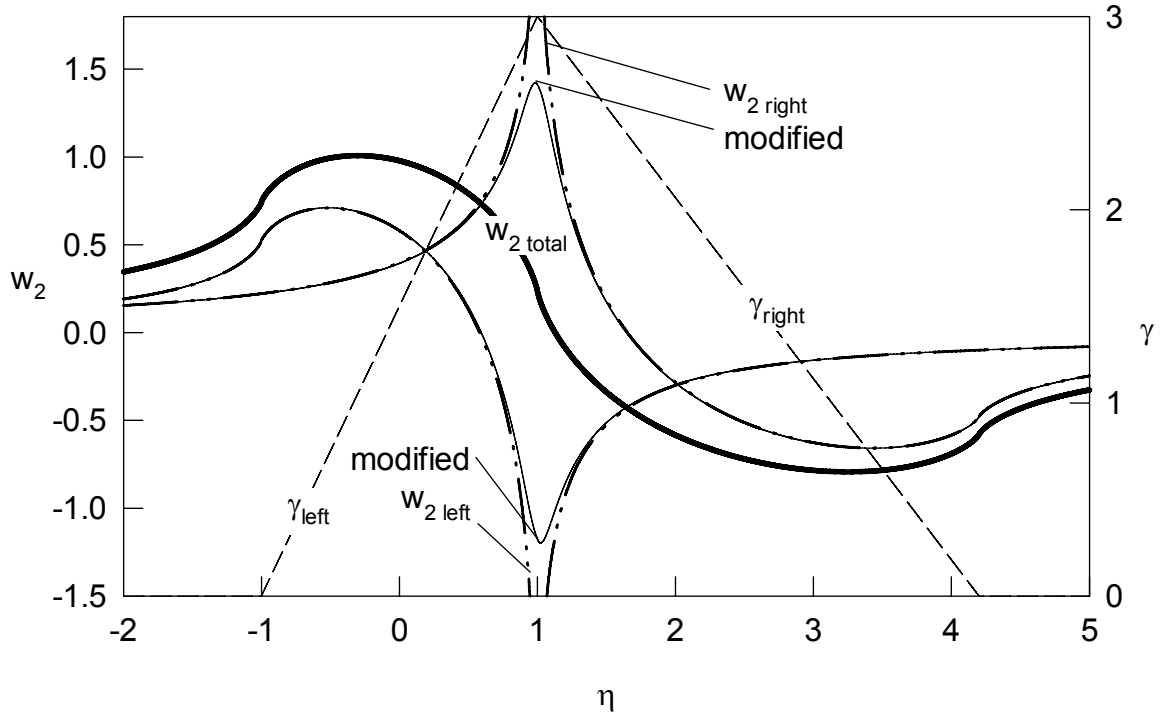
Figure 9: A spanwise distribution of the normal velocity that is induced in the plane of two semi-infinite vortex sheets. The "left" sheet spans from η = -1 to 1, the "right" one from η = 1 to 4.2. The dashed line denotes the spanwise vorticity distributions, the solid line the total induced velocity.

Although the singularities along the side edges of a semi-infinite vortex sheet have little effect on the overall induced velocity of a larger vortex-sheet system whose continuous vorticity distribution is modeled with several such semi-infinite vortex sheets, the numerical implementation of such a discretized model requires further treatment of the logarithmic terms in Eq. 7. One possible approach is to add an additional singularity to either side edge of an individual semi-infinite vortex sheet in order to cancel the original singularities. Overall, in combination with the original and the added singularities of the neighboring vortex sheets, all the singularities cancel each other and the combined induced

33

velocity remains unaffected. Adding additional singularities to either side edge of a vortex sheet modifies the logarithmic term of Eq. 7:

$$w_2(\eta_0) \sim \ln\left[\frac{k+(\eta_0-\eta_i)^2}{k+(\eta_0+\eta_i)^2}\right]$$

(8)

where k is a positive constant. As a result of this modification, the velocity that is induced by a vortex sheet remains finite, even along the side edges of the sheet, as indicated by the "modified" induced velocities in Fig. 9. Despite the changes to the individually induced velocities, the combined velocity, $w_{2\,total}$, remains unchanged. This "modification" is included in the complete solution of the integral equation of Eq. 6 that is listed in Appendix 2.

The rate at which the influence of the additional singularity diminishes with increasing distance to its location depends on the size of the constant k. A smaller k reduces the impact on the induced flow field further away, but also increases the induced velocity peak at the edge itself. Either "modified" induced velocity distribution displays such a peak at $\eta = 1$. The lessening of the impact further away is especially an issue in order to minimize the impact of the additional singularity that is located at a wingtip. Unless the vorticity is zero at the wingtip, which despite the circulation being zero, is usually not the case, the vortex sheet at the wingtip has the only additionally introduced singularity that is "unbalanced" by a neighboring vortex sheet. Its influence can significantly affect the entire circulation distribution by distorting the flow field at the control points further inboard. In contrast to that, the induced velocity peak is a concern when computing the local velocity at a side edge of a vortex sheet that has an

"unbalanced" newly introduced singularity. This can occur when two neighboring vortex sheets align improperly, for example, due to panel leakage. More commonly, the velocity peak becomes an issue in the wake downstream of a wingtip where, for example, the local velocity peak of the "unbalanced" singularity of the tip might distort the wake-relaxation process.

A k-value of one-percent of the vortex-sheet half-span has yielded good results in the computed overall velocity distribution. This value reduces the impact on the circulation distribution to a minimum without causing major local velocity peaks in the flow field. The latter is helped by the fact that the locally computed flow field is the composition of the influences of many vortex-sheet elements.

The above-described treatment of the singularities along the side edges of a vortex sheet allows the numerical representation of a first-order continuous vortex sheet using vortex-sheet elements that have linear spanwise vorticity distributions. The velocities that such a modeled continuous vorticity distribution induces are finite everywhere. Although the tangential velocity is undetermined in the plane of the sheet, in a numerical implementation it can be averaged with the finite velocity values that are present just above and below the sheet. The leading edge singularity of a swept semi-infinite vortex sheet is treated in the same way as are the side edges, that is by introducing an additional singularity in order to cancel the original one.

3.2   Distributed Vorticity Elements

In the method presented here, the lifting surfaces and the wake are modeled using what are termed here as distributed vorticity elements. As shown in Fig. 10, a distributed vorticity element has vortex filaments along its leading and trailing edges. These filaments have spanwise circulation distributions that are parabolic and of opposite orientations. Between these filaments, a vortex sheet with a linear spanwise vorticity distribution satisfies the Helmholtz vortex theorem. The vorticity of the sheet is aligned with one of the primary local axes, the ξ-axis, which is oriented along the local flow direction. The sheet lies in the ξ-η plane and, thus, the ζ-axis is normal to the plane of the vortex sheet of the distributed vorticity element. The reference point, $\underline{x}_0$, that is located at the geometric center of the element serves as the origin of the local ξ-η-ζ-reference frame. The vortex filaments at the leading and trailing edges intersect the η-axis at the respective sweep angles, $\varphi_{l.e.}$ and $\varphi_{t.e.}$. The two sides of the element are parallel to the ξ-axis. The span, $2\eta_i$, is the shortest distance between the sides, and the chord, $2\xi_i$, is measured along the centerline of the element.
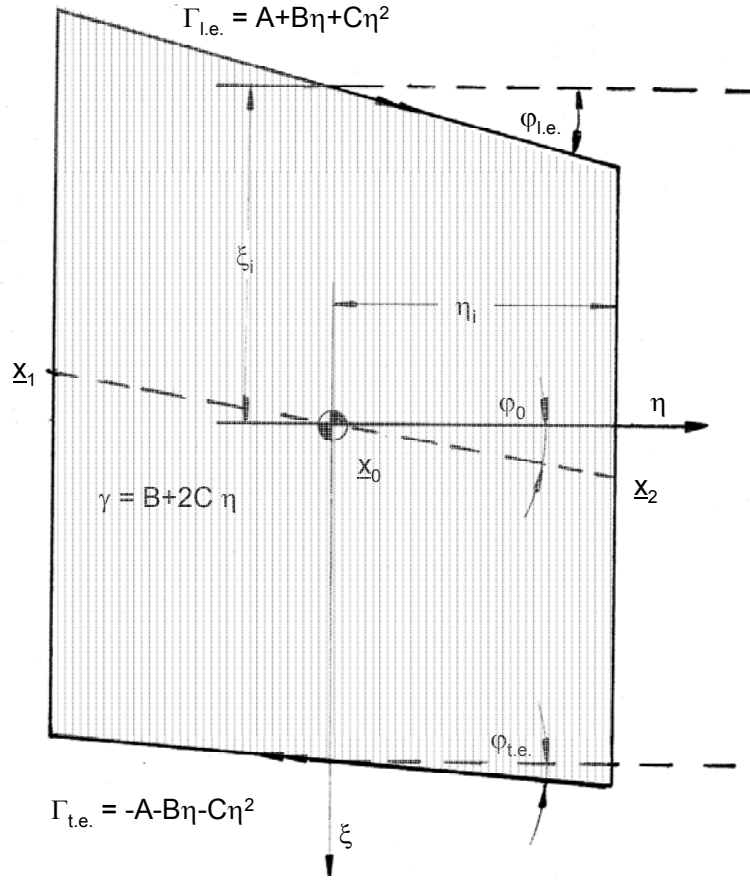
Figure 10: The distributed vorticity element.

Three rotations relate the global reference frame to the local one: the dihedral angle, ν, about the x-axis, the incidence angle, ε, about the y'-axis, and the yaw angle, ψ, about the z"-axis. All coordinate systems are right-hand systems. Based on this convention the following coordinate transformation relates the wing-fixed reference frame to that of the local distributed-vorticity element:

$$\begin{bmatrix} \xi \\ \eta \\ \zeta \end{bmatrix} = \begin{bmatrix} \cos\psi\,\cos\varepsilon & \cos\psi\,\sin\varepsilon\,\sin\nu + \sin\psi\,\cos\nu & -\cos\psi\,\sin\varepsilon\,\cos\nu + \sin\psi\,\sin\nu \\ -\sin\psi\,\cos\varepsilon & -\sin\psi\,\sin\varepsilon\,\sin\nu + \cos\psi\,\cos\nu & \sin\psi\,\sin\varepsilon\,\cos\nu + \cos\psi\,\sin\nu \\ \sin\varepsilon & -\cos\varepsilon\,\sin\nu & \cos\varepsilon\,\cos\nu \end{bmatrix} \begin{bmatrix} x-x_0 \\ y-y_0 \\ z-z_0 \end{bmatrix}$$

(9)

The inverse transformation is:

$$\begin{bmatrix} x \\ y \\ z \end{bmatrix} = \begin{bmatrix} \cos\psi\,\cos\varepsilon & -\sin\psi\,\cos\varepsilon & \sin\varepsilon \\ \cos\psi\,\sin\varepsilon\,\sin v + \sin\psi\,\cos v & -\sin\psi\,\sin\varepsilon\,\sin v + \cos\psi\,\cos v & -\cos\varepsilon\,\sin v \\ -\cos\psi\,\sin\varepsilon\,\cos v + \sin\psi\,\sin v & \sin\psi\,\sin\varepsilon\,\cos v + \cos\psi\,\sin v & \cos\varepsilon\,\cos v \end{bmatrix} \begin{bmatrix} \xi \\ \eta \\ \zeta \end{bmatrix} + \begin{bmatrix} x_0 \\ y_0 \\ z_0 \end{bmatrix}$$

$$(10)$$

Two points of significance are the mid-chord locations of the left and right side edge of the distributed vorticity element, $\underline{x}_1$ and $\underline{x}_2$, respectively. In the local reference frame of the distributed vorticity element, these points have the following coordinates:

$$\underline{x}_1 = \begin{bmatrix} -\eta_i \tan\varphi_0 \\ -\eta_i \\ 0 \end{bmatrix} \qquad (11\ a)$$

and

$$\underline{x}_2 = \begin{bmatrix} \eta_i \tan\varphi_0 \\ \eta_i \\ 0 \end{bmatrix} \qquad (11\ b)$$

where φ_0 is mid-chord sweep angle.

Numerically, the velocity that such a distributed vorticity element induces at a given point is composed of the influences of two vortex filaments and two semi-infinite vortex sheets. As shown in Fig. 11, one vortex filament and one semi-infinite vortex sheet begin at the leading edge of the distributed vorticity element. The second set that has the opposite circulation and vorticity distribution, begins at the trailing edge of the element. Consequently, the two vortex sheets cancel each other downstream of the trailing edge. The subsequent induced velocities are computed with the analytical solutions of Eqs. 5 and 6,[28] modified in accordance with Eq. 8, in order to manage the singularities

along the edges of the distributed vorticity element. A more detailed description
of the induced velocity calculation is given in Appendix 3.
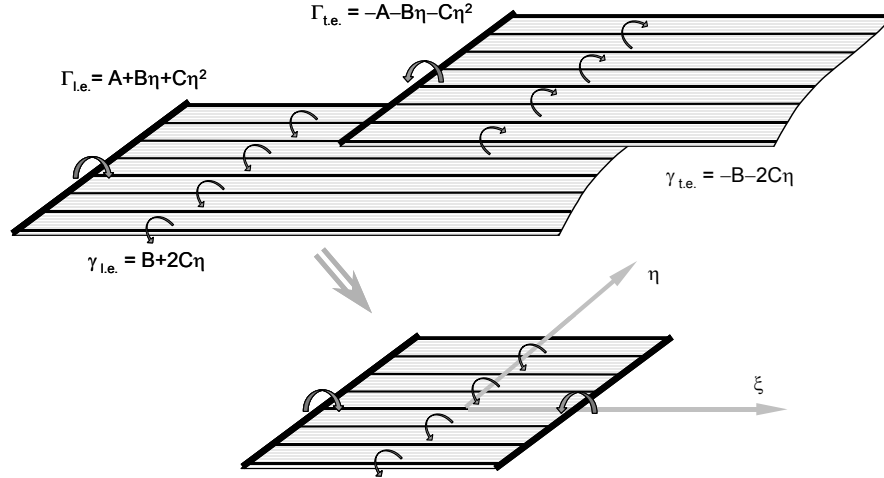
Figure 11: A distributed vorticity element is composed of vortex filaments along
its leading and trailing edges, as well as of two semi-infinite vortex sheets.

3.2.1 The Lifting Surface

A lifting surface is modeled using distributed vorticity elements similarly to
how it is done in the multiple lifting-line method.[28] In the spanwise direction, the
parabolic circulation distributions of the vortex filaments form a second-order
spline. The subsequent vortex sheets between the leading and trailing edge
filaments have a continuous spanwise vorticity distribution that is a first-order
spline. Several such spanwise systems can be positioned at different chordwise
locations, as shown in Fig. 12.

The circulation coefficients of each distributed vorticity element, A, B, and
C, are determined by solving a system of linear equations that satisfies three
boundary conditions. One of the boundary conditions is the requirement for flow
tangency at the center of each distributed vorticity element. The two additional

39

boundary conditions are provided by the need to maintain a continuous circulation and vorticity in the spanwise direction across the boundaries of each distributed vorticity element. A more detailed description of the system of linear equations, whose solution holds the bound circulation distribution, is included in Appendix 4.

As is the case with panel methods, it is possible to model thickness by placing distributed vorticity elements around the contour of the wing. In this study, however, the elements are distributed over the chord, or zero-lift, surface in order to limit the computing time. Thus, it is essentially a vortex-lattice method, as it is shown in Fig. 12. In the example presented there, the wing is modeled using three elements across the half-span and two along the chord. Similar to the vortex-lattice method shown in Fig. 4, the leading edge-vortex filament of each distributed vorticity element is located at the quarter-chord location of that particular element. Its trailing edge filament, however, coincides with the location of the leading edge filament of the next element downstream. The surface elements that are located along the trailing edge of the wing reach into the wake in order to satisfy the Kutta condition.
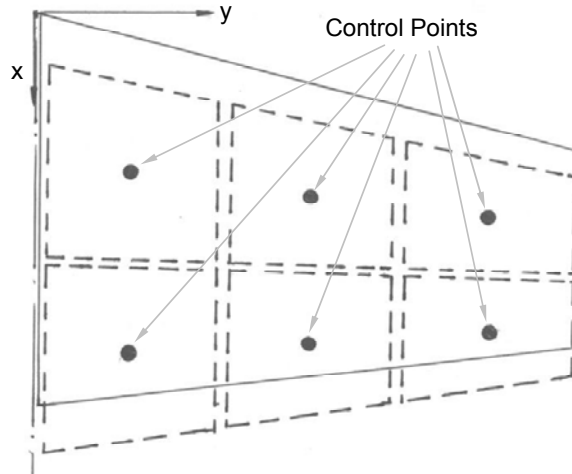
Figure 12: Paneling of the lifting surface (solid lines) with distributed vorticity elements (dashed lines).

Leakage may occur between the distributed vorticity elements of a lifting surface that has twist, since the elements remain planar and are, in fact, only truly continuous in the spanwise direction along their leading edge-vortex filaments. Nevertheless, the amount of leakage will be limited and negligible if a sufficient number of spanwise panels is used.

3.2.2 The Wake

The wake model with distributed vorticity elements is similar to that of the lifting-surface. In order to reduce the computational effort and eliminate singularities, however, the leading and trailing vortex filaments are omitted. This is permissible under steady-state conditions with constant streamwise vorticity distributions.

The wake shape is developed using a time-stepping method.[17] As the wing progresses forward each time step, a new spanwise row of distributed vorticity elements is emitted from the trailing edge into the wake. The vorticity

41

distribution of the wake elements depends on the strength of the circulation of the surface elements that are located along the trailing edge. Depending on the trailing edge shape and the direction of motion, the wake elements are trapezoidal and planar in shape. The spanwise row of elements that has been released into the wake during the first time step consists of semi-infinite vortex sheets that are aligned with the free stream velocity. This expedites the convergence of the forces during the time-stepping method.

In order to achieve a force-free wake, the distributed vorticity elements are displaced with the local velocity, $\underline{u}_{ind}$, during each time step. Consequently, the displacement is $\underline{u}_{ind} \Delta t$, where Δt is the time-step size. More specifically, the mid-chord points at the side edges of each distributed vorticity element, $\underline{x}_1$ and $\underline{x}_2$ in Fig. 10, are displaced along the local induced flow field. The new reference point is placed between the new locations of the side-edge points, $\underline{x}_1$ and $\underline{x}_2$. Their relative location to each other also defines the new roll attitude of the element, as well as its new span, η_i. The new pitch attitude depends on the relative vector between the new reference point and the midspan location of the trailing edge of the next upstream element. Despite stretching and tilting during the wake roll-up process, each wake element remains planar.

As the wake elements are stretched and compressed, their vorticity distribution must be adjusted for the change in span to satisfy the Helmholtz theorem. This theorem requires that the total circulation be unchanged. Thus, in the particular case of a distributed vorticity element, the following integral must remain constant:

$$\frac{1}{2\eta_i} \int_{-\eta_i}^{\eta_i} \Gamma(\eta) \, d\eta = \text{const.} \tag{12}$$

where η_i is the half span of the distributed vorticity element with its spanwise

circulation distribution $\Gamma(\eta)$. This condition and the two additional requirements

of continuous circulation and vorticity distributions across the spanwise

boundaries between the distributed vorticity elements allows the formulation of a

linear equation system whose solution yields the "stretched" circulation-

distribution coefficients, A, B, and C. Under steady conditions, to satisfy the

Helmholtz theorem in the streamwise direction, the integral value of Eq. 12 is

constant for the wake elements of a particular span location. It depends on the

value of the surface element of that particular span location that is located at the

trailing edge of the lifting surface.

Similar to the lifting surface, leakage can occur between the wake

elements, which remain planar as they rotate and stretch during the relaxation

process. This, however, only becomes an issue when computing the local

velocities in such a gap between wake elements. In such a case, the velocity

peaks that are induced by the edge of one distributed vorticity element may be

unbalanced. Although this particular contribution to the total induced velocity is

finite, it may nevertheless be large compared to the contributions of the

remaining flow field. Thus, in order to minimize any such problems during the

relaxation process, the wake elements are attached in the spanwise direction at

their mid-chord locations and in the streamwise direction at their midspan

locations. Downstream of the wingtip, however, the distributed vorticity elements

in the wake display velocity peaks that are self-induced and are due to the unbalanced singularities at the edge of the wake. For example as shown in Fig. 9, the induced velocity of each individual vortex sheet peaks at $\eta=1$. Although these peaks cancel in the presence of a neighboring element, this is not the case at the tips of the wing and wake. Fortunately, the influence of this self-induced velocity peak on the role-up behavior is limited, in that, the self-induced contribution is only part of the total induced velocity that is the result of the induction by the entire wake and the lifting surface.

3.3   Forces

The normal force of a lifting surface is the sum of all the forces that arise from the Kutta-Joukowsky law being applied at each vortex filament of the surface elements. The force is comprised of a part due to the free-stream flow and one due to the induced velocity. The free-stream force-contribution uses an analytical solution to integrate the lift force across the span of each bound vortex.[28] The induced lift of each surface element is determined with a numerical integration. Using Simpson's rule for this integration requires that the locally induced velocities be determined at three locations along the bound-vortex span of the surface element. The three locations are at the midspan and at $0.8\eta_i$ on either side of it. The choice of the latter two points eliminates the chance of issues with the singularities at the edges of each surface element.

The induced drag is computed in a manner similar to that of the induced lift by applying the Kutta-Joukowsky law along the trailing edge of the lifting

surface. To do this, the cross product is taken between the circulation that is

shed into the wake at the trailing edge and the velocity that the wake induces

there.[38,40,43] The total drag force is determined using a numerical spanwise

integration, just as it is done for the induced lift. As can be observed in Fig. 13,

the results agree well with those obtained using an analytical approach in the

Trefftz plane. The figure shows the forces and span efficiencies computed using

the multiple lifting-line method of Ref. 28. The drag forces of the wing that has

an elliptical chord distribution and a straight trailing edge are computed in the

Trefftz plane as well as along the trailing edge as discussed in Ref. 38. As the

number of spanwise panels varies, the two drag-calculation methods and the

subsequent span efficiencies display differences that are less than half of a

percent.
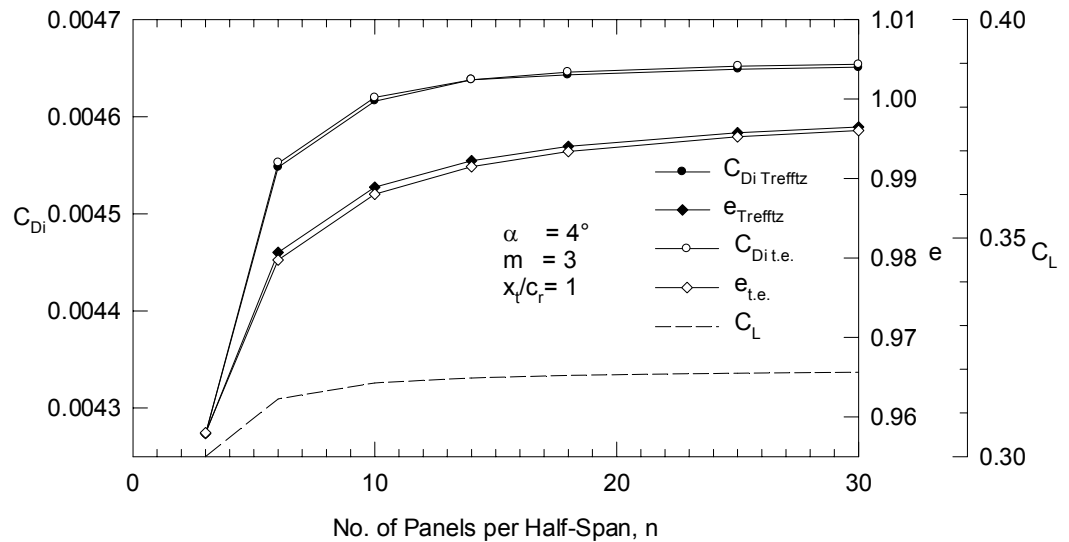
Figure 13: Forces and span efficiencies of an elliptical wing with a straight
trailing edge computed using the multiple lifting-line method.[28] The induced drag
is computed in the Trefftz-plane and by applying the Kutta-Joukowsky law along
the trailing edge of the wing.

45

Special attention is required when determining the induced drag of a wing with a swept trailing edge. In that case, the normal velocity that the shed semi-infinite vortex sheet induces along the swept line is singular.[28] In spite of the singular velocity, the induced drag, which is the spanwise integral of the cross product of the induced normal velocity and the lumped circulation, is finite.[37] Indeed, as discussed in Chapter 2.4, the induced drag of the swept wing is identical to the one of an unswept wing with the same spanwise circulation distribution.[12,37] An example of this is shown in Fig. 14, which shows the forces and span efficiencies of wings with elliptical chord distributions and varying sweeps. $x_t/c_r = 0$ denotes a straight leading edge, whereas $x_t/c_r = 0.25$ is a straight quarter-chord line, and $x_t/c_r = 1$ a straight trailing edge. The drag force in the Trefftz plane and the lift force were computed using the multiple lifting-line method of Ref. 28. In addition, the drag force was computed using the Kutta-Joukowsky theorem along a "de-swept" trailing edge. Despite the varying sweeps, the far and near field results of the two agree well. The near field method, however, is much more suitable for a relaxed wake than a Trefftz-plane integration. The latter requires the knowledge of the exact shape of the shear layer far away from the lifting surface and is relatively sensitive to even small shape changes.[44] In comparison to that, the drag estimation along the trailing edge is less dependent on the numerical accuracy of an "aged" wake that is distant from the lifting surface of interest.
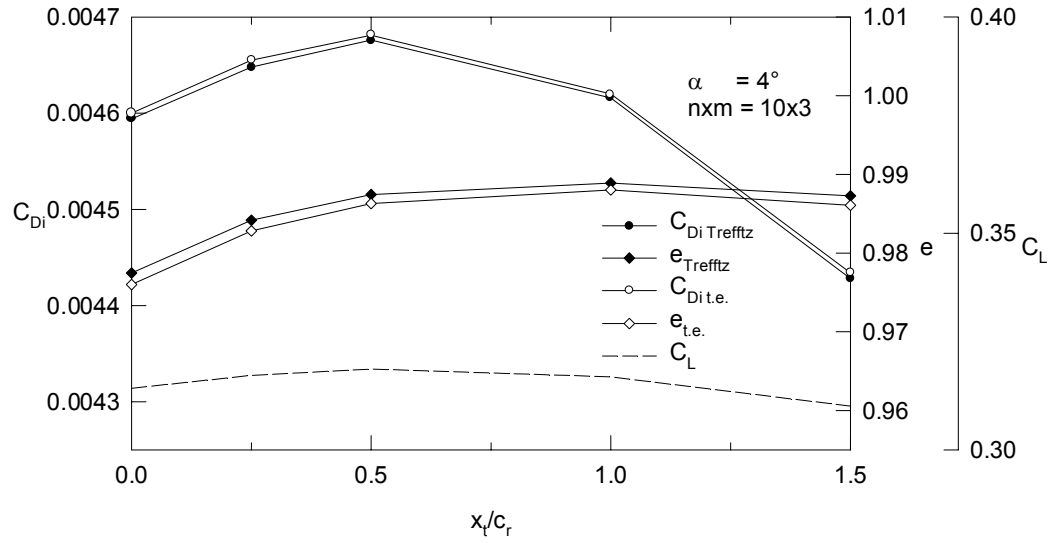
Figure 14: Forces and span efficiencies of the multiple lifting-line method[28] using results from the Trefftz-plane and Kutta-Joukowsky along the trailing edge of a wing with an elliptical chord distribution and varying trailing-edge sweeps.

4   Validation

This section deals with the validation of the method introduced in Chapter 3. The primary interest is the accuracy in forces and wake-shape prediction. Three basic criteria are considered for the accuracy assessment in this section.

First, the model has to realistically represent the particular physical problem in its geometry and boundary conditions. In the case of the newly developed method, the potential flow problem of the wing and its trailing wake allows the investigation of the physical events of interests: induced drag and the flow field in the wake.

The second accuracy criterion requires that the computed solutions be insensitive to input parameter changes, such as the variation of the panel density. In addition the convergence behavior of the method must be robust. This means that, if the posed problem is a steady one, the long-term computational solution, once it has converged, should approach a constant value.

A third accuracy assessment is how well the results of the new method compare with results attained using other methods. These results can be theoretical, computational, or experimental in nature. In this study, the classical lifting-line theory results of an elliptical lift distribution having a span efficiency of 1.0 serves as a benchmark for the force prediction of the elliptically-loaded wing. Additionally, a comparison of the computed loads is performed with other numerical methods. Beyond that, the computed flow fields behind wings are compared with experimental results. Whereas the results of the classical lifting-

line theory and the other numerical methods are inviscid, the experiments are subject to viscous effects, especially for the flow over the lifting surface. This makes a comparison of drag forces difficult, since a separation of viscous from inviscid drags is difficult in the experiments. In the wake, however, the viscous effects subside within a short distance behind the trailing edge of the wing, and the wake is largely inviscid. Thus, if the experimental and theoretical bound vorticity distributions of the wings match, the shed vorticities should produce similar flow fields in the wake.

4.1   The Elliptical Wing

In order to validate the method described in the previous section, the forces on wings having elliptical chord distributions were computed and compared with results obtained elsewhere.[28,44,45] The elliptical planforms considered have aspect ratios of 7 and various amounts of sweep. An angle attack of 4 degrees is used, which corresponds to a cruise-lift coefficient of approximately 0.32. The distributed vorticity elements are distributed linearly along the span and the chord of the lifting surface.
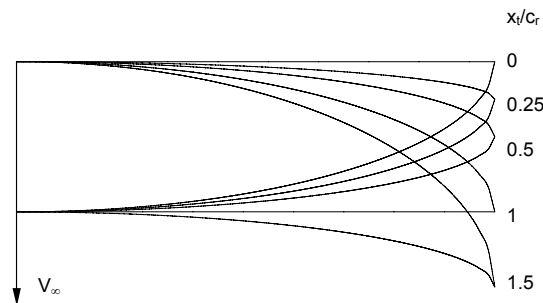
Figure 15: Elliptical planforms with various tip locations.

The respective planforms are shown in Fig. 15, where $x_t/c_r = 0$ denotes the wing with an unswept leading edge, and $x_t/c_r = 1$ is the crescent wing that has an unswept trailing edge. Only the latter planform has a fixed, drag-free wake that has a planar trace in the Trefftz plane independently of angle of attack. In comparison, the straight wake shed from the forward swept trailing edge of the classical elliptical wing, that is $x_t/c_r = 0.25$, has growing dihedral with increasing angles of attack. Its subsequent trace in the Trefftz plane has an elliptical dihedral distribution. Conversely, the Trefftz-plane projection of an aft-swept trailing edge has anhedral with positive angles of attack. Thus, the elliptical planform with a straight trailing edge matches most closely the assumptions made in the classical lifting-line theory regarding a planform having an elliptical circulation distribution.

4.2   Convergence Study

The wake is developed using a time-stepping method and, consequently, the strength of the shed vorticity changes dramatically in the early stage of the wake evolution. The convergence behaviors of induced drag coefficient, lift coefficient, and the span efficiency are shown in Fig. 16 for different step sizes in the wake for a wing with an elliptical chord distribution and a straight trailing edge, $x_t/c_r = 1$. The lifting surface was modeled with mxn = 18X3 distributed vorticity elements across the halfspan and the chord, respectively. Three different wakestep sizes were used in order to develop the relaxed, force-free wake: 0.5, 1, and 2 percent of the wingspan. Also shown in the figure is the convergence behavior of the equivalent values of a fixed, drag-free wake that is

50

shed from the trailing edge of the wing along the direction of the free stream. This is in contrast to the multiple lifting-line method of Ref. 28, whose wake is shed from the lifting line.

The fixed wake model reaches its converged values after approximately 20 time steps, whereas the relaxed wake models require roughly 60. Any oscillatory behavior is strongly dampened with the exception of occasional peaks of the relaxed wake model that uses the smallest step size of 0.5 percent of the wingspan. Although these outliers are most likely the result of leakage issues in the relaxed wake, it is significant to notice that they remain limited in value. Overall, the convergence behavior is numerically well behaved and the converged forces are relatively independent and robust to the choice of step size in the wake. Within the first 20 time steps, all models are within half-a-percent of their converged value.

The computation time required for the results that are discussed above is plotted at the top of Fig. 16. The computations were performed on a computer with dual GenuineIntel processors with processing speeds of 3 Ghz. The computational time increases exponentially as the number of wake elements grows with each time step. Despite the need of nearly five days for the simulation of 500 time steps, 20 and 60 time steps only require approximately 5 and 47 minutes, respectively.

Based on these results and in order to speed up the simulations, the results that are discussed in the following sections were computed with wakes

that were modeled with at least 60-time steps, each of which was set to 2 percent

of the wingspan in streamwise direction.
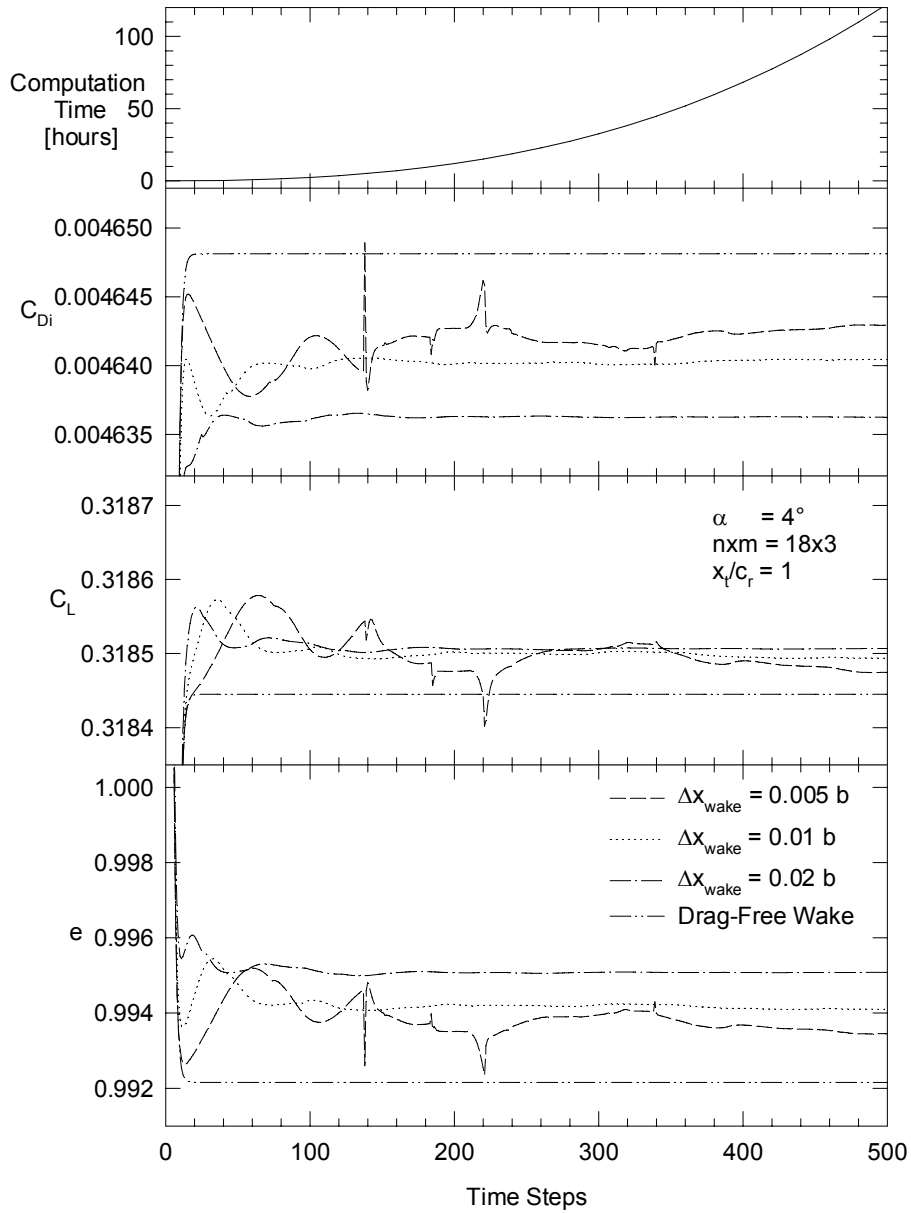
Figure 16: Convergence behavior of drag and lift forces, as well as span-efficiency factor of a wing with an elliptical chord distribution and straight trailing edge using various step sizes in the relaxed wake.

4.3   Panel-Density Effects

The influence of the spanwise paneling density on lift and drag coefficients and the span efficiency is shown in Fig. 17. The wing has an elliptical planform with a straight trailing edge and an aspect ratio of seven. The linear spanwise panel distribution varies from 3 to 30 panels per halfspan, with three panels used along the chordwise direction of the lifting surface. The force and span-efficiency values rise asymptotically with an increasing number of spanwise panels. Although lift and drag appear to be leveling off at the higher panel density in the spanwise direction, the span-efficiency factor keeps approaching the theoretical value of one.
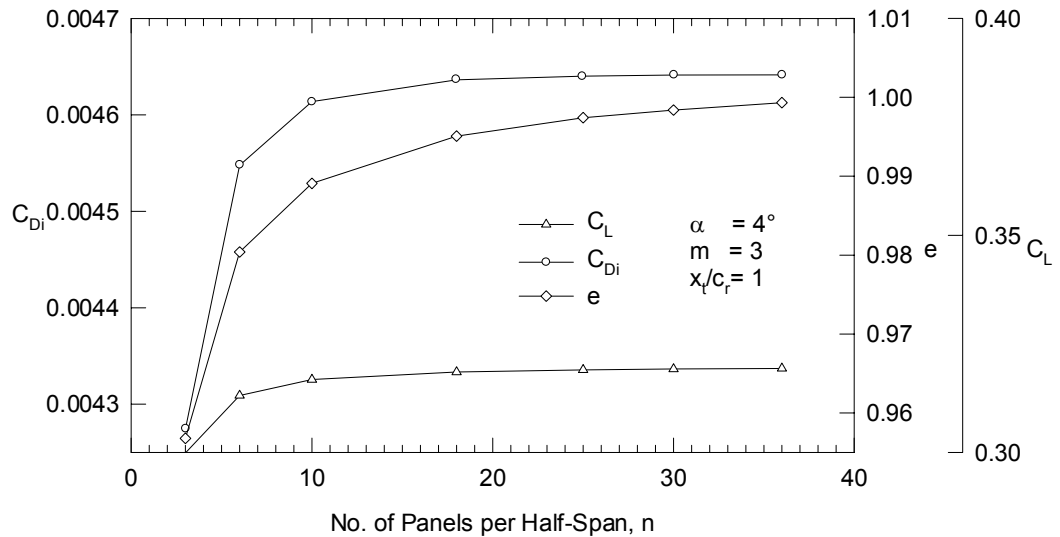
Figure 17: Behavior of lift, drag and span efficiency as function of varying panel density in spanwise direction of a wing with an elliptical chord distribution and straight trailing edge.

The effect of varying the panel density in chordwise direction is shown in Fig. 18. The linear chordwise distribution is increased from 1 to 10 panels. The spanwise panel density is 18 panels across the halfspan of the wing. The

computed values are relatively constant for three or more panels in the chordwise direction.
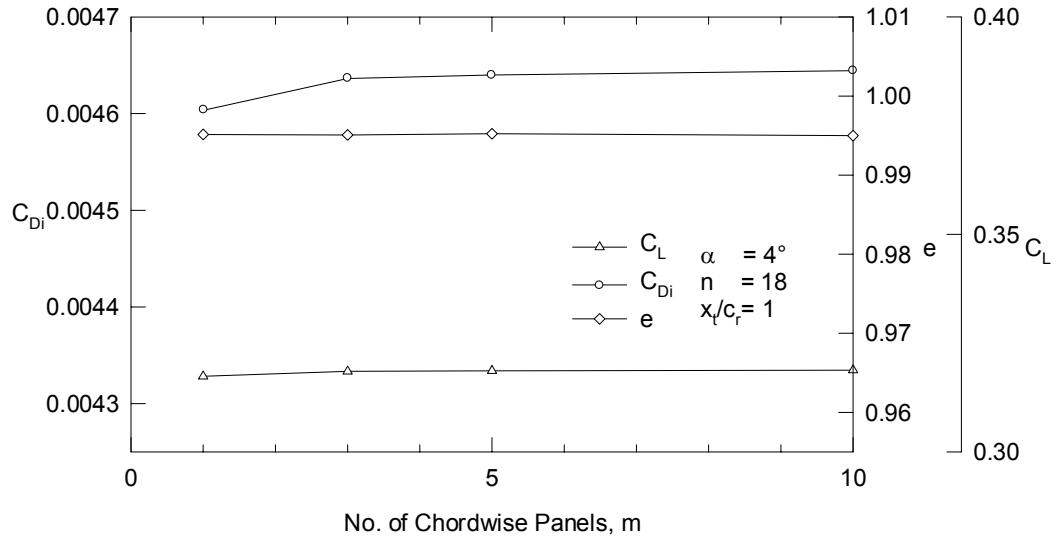
Figure 18: Behavior of lift, drag and span efficiency as function of varying panel density in chordwise direction of a wing with an elliptical chord distribution and straight trailing edge.

4.4 Angle of Attack Effects

The influence of the angle of attack on the span efficiency is shown in Fig. 19. Besides the results that were obtained with the relaxed, force-free wake model that uses distributed vorticity elements (thus denoted with subscript DVE), the figure also shows the values derived using the multiple lifting-line method of Ref. 28. In the latter case, the span efficiency was computed using two different methods that compute the induced drag either in the Trefftz plane[28] or along the trailing edge of the wing.[38] Theoretically, the span efficiency of the elliptical wing with a straight trailing edge is unaffected by the change in angle of attack. In the numerical application, however, a change is likely to occur at small angles of attack due to inaccuracies in computing the small aerodynamic loads. The span

efficiencies of the three models are very similar in value and are relatively

insensitive towards changes in the angle of attack. The results of the fixed wake

models remain constant, whereas the relaxed wake model displays a drop off at

higher angle of attacks most likely due to the influence of a more strongly rolled-

up wake.
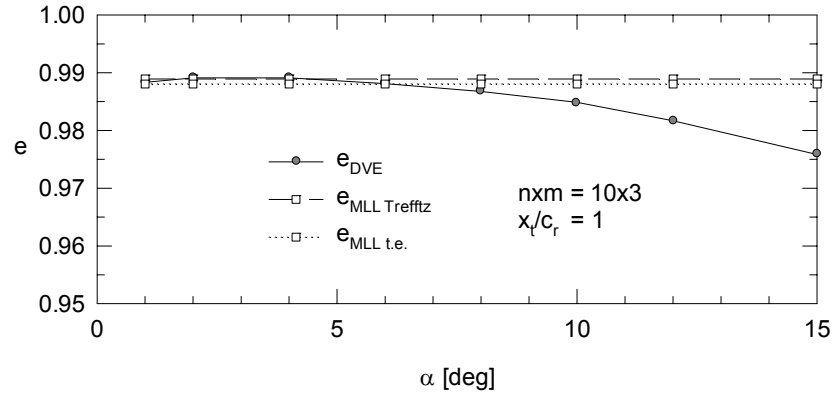
Figure 19: Effect of angle of attack on the span-efficiency factor of a wing with an elliptical chord distribution and straight trailing edge; comparison of results of the relaxed, force-free model and the multiple lifting-line method of Ref. 28, denoted DVE and MLL respectively.

4.5   Lift Distribution

The spanwise lift distribution for case of the wing with an elliptical chord

distribution and a straight trailing edge is plotted in Fig. 20. The lifting surface is

modeled with 10, 18, and 36 distributed vorticity elements along the span and

three along the chord. Also plotted in this figure is the theoretical case of an

elliptical lift distribution. The differences between theory and the calculated

solution are small and occur mainly in the very tip region, where the second-

order splines of the models fail to follow the infinite slope of the theory. In order

to better demonstrate the agreement of the computational method with the

theory, the spanwise distributions of the section-lift coefficients are also plotted in Fig 20. The theoretical case, which would be a constant line, is not plotted in this figure. The calculated values of the wing with elliptical chord distribution match well the theory and remain constant over most of the span. Only near the wingtip, the calculated values deviate noticeably from the theory, especially in the cases with lesser spanwise panel densities.
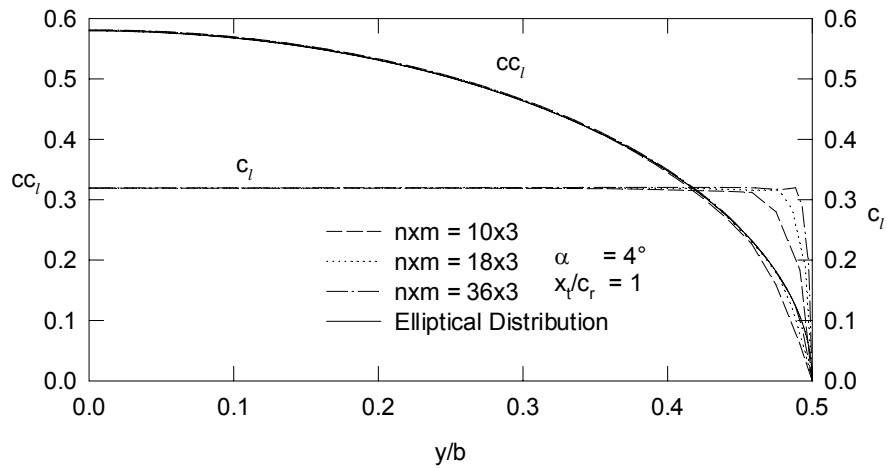
Figure 20: Comparison of spanwise distribution of lift and lift coefficient of an elliptical wing with aspect ratio 7 and different panel densities.

An example of the chordwise load distribution is shown in Fig. 21 for the center section of the wing with an elliptical chord distribution. The number of distributed vorticity elements in chordwise direction is 3, 5, and 10. In spanwise direction, 18 distributed vorticity elements were used across the halfspan of the lifting surface. The local section-lift coefficients essentially represent a discretized solution of the differential pressure coefficients between upper and lower surface of a flat plate. Thus for comparison reasons, the solution arising from thin airfoil is also plotted in this graph. The discrete models using

distributed vorticity elements agree well with the theory. As it is to be expected, the results obtained using the higher numbers of chordwise elements are in better agreement with the thin airfoil-theory results. Differences occur mainly towards the leading edge, at which point the analytical solution approaches infinity.
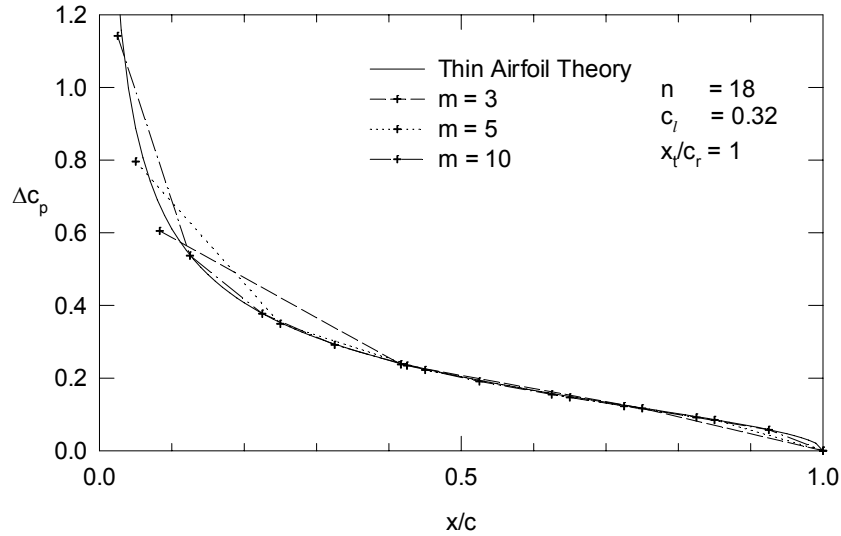
Figure 21: Comparison of the theoretical chordwise load distribution of a flat plate and the chordwise load distribution at the center section of an elliptical wing with aspect ratio 7 that was modeled using distributed vorticity elements.

4.6 Comparison with Other Methods

The influence of different planforms with elliptical chord distributions on the span-efficiency factor is shown Fig. 22. In this figure, the results of the relaxed wake method that uses distributed vorticity elements are compared with the results of other references. As discussed in Chapter 2.2.4, the multiple lifting-line method of Ref. 28 uses a second-order spline for the spanwise distribution of the bound circulation. Its subsequent drag-free wake is modeled with semi-infinite vortex sheets that have linear vorticity distributions. The drag is

determined along the trailing edge, the result of which agrees well with the Trefftz-plane drag-results, as it has been demonstrated in Figs. 13 and 14. The results of Ref. 44 were derived with a panel code using a force-free and a drag-free wake model. The method uses higher-order panels for modeling the lifting surface and discrete vortex filaments with solid cores in the wake. Induced drag is computed in the Trefftz-plane after converting the wake-vortex filaments into panels whose doublet strengths vary piecewise linearly in the spanwise direction. In comparison to the method of Ref. 44, the drag and lift forces of the higher-order panel-code of Ref. 45 were computed using a surface-pressure integration. Similar to the herein introduced method, the code of Ref. 45 models the lifting surface and the wake with higher-order elements. The results of Ref. 40 were derived with a panel method that models the force-free wake using discrete potential vortices. The induced drag was computed along the trailing edge, in a similar manner as done in the higher-order lifting surface method that is introduced here.

Overall, the different methods agree well over the range of investigated wingtip locations. The force-free results of the distributed vorticity-element method are in good agreement with the results of the drag-free wake-models of Refs. 28 and 44. The results of the latter case, however, deviate increasingly with more aft wingtip locations. In that region, the results obtained with the method using distributed vorticity elements are in better agreement with those of the force-free wake-results of Refs. 40, 44, and 45. Although the method introduced here agrees well with the drag-free results of Refs. 28 and 44 in the

case of the unswept quarter-chord line, $x_t/c_r=0.25$, noticeably small differences of less then two percent exist when compared with the results of the three relaxed-wake methods of Refs. 40, 44, and 45. Varying the panel density of the lifting surface and in the wake of the distributed vortex-element method has no apparent influence on these small differences. Thus, it is assumed that the differences are inherent to the methods, for example due to thickness effects.

The new method that uses distributed vorticity elements clearly requires fewer elements in the spanwise direction in order to achieve an accuracy that is similar to the other relaxed wake models of Refs. 40, 44, and 45. In addition, the induced drag computation using the method of Ref. 38 is less sensitive to changes in the panel density of the lifting surface and the wake.
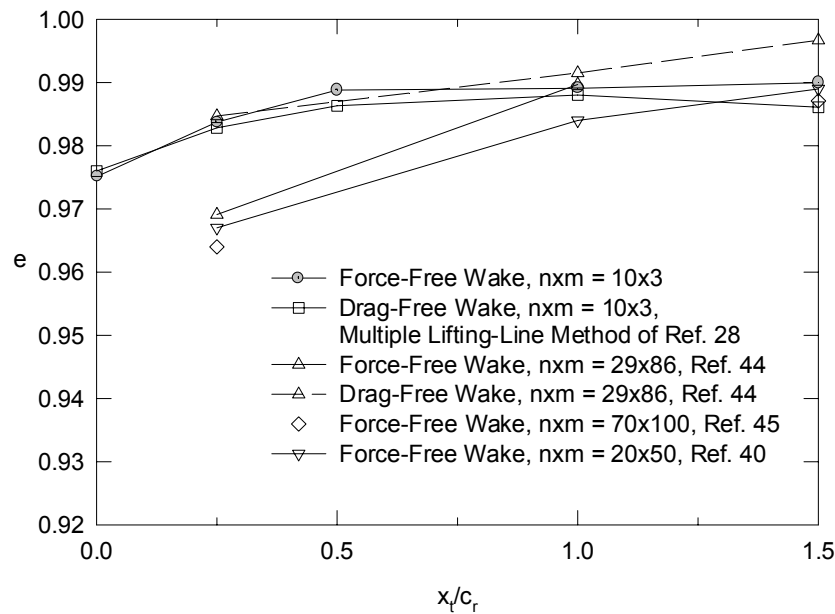
Figure 22: Effect of tip location on the span-efficiency factor of a wing with an elliptical chord distribution at a lift coefficient of approximately 0.33; comparison of results derived with the relaxed, force-free model using distributed vorticity elements and other methods of various references.

59

4.7   Comparison with Experimental Results

It is difficult to distinguish induced drag from the overall drag of an experiment. Even the adjustment with skin-friction and pressure drag assumptions is likely to have larger inaccuracies than is required for the assessment of a potential flow method. Thus, in order to assess the new method that uses distributed vorticity elements, other physically measurable phenomena are used for comparison purposes. Such observable facts are, for example, the shapes of the shear layers in the wake, the circulation in the rolled-up tip vortex, and crossflow velocity fields.

4.7.1   Shear-Layer Shape

One of the objectives of the method presented herein is to predict the shape of the wake accurately. A comparison between experimental[46,47] and computational results of the wake shapes that are shed by a rectangular wing with an aspect ratio of 2.4 is shown in Fig. 23. In this figure, the calculated shear-layer cross-sections of the wake are superimposed onto the corresponding photographic results presented in Ref. 46. The wing of the computation model was modeled with one row of 42 distributed vorticity elements in spanwise direction. The wake extends for 250-time steps 12.5 spans downstream. The original photograph was produced using hydrogen bubbles to visualize the shear layer of the wake coming of the wing. In the experiment, the wake separates from the wing surface just aft of the mid-chord.[46,47] The angle of attack is 9 degrees. Although the shed vortex sheet is initially turbulent, it has largely

60

relaminarized at the locations of the pictures in Fig. 23, which are 5.5, 11.2, and 21-chord lengths downstream of the trailing edge.[46,47]
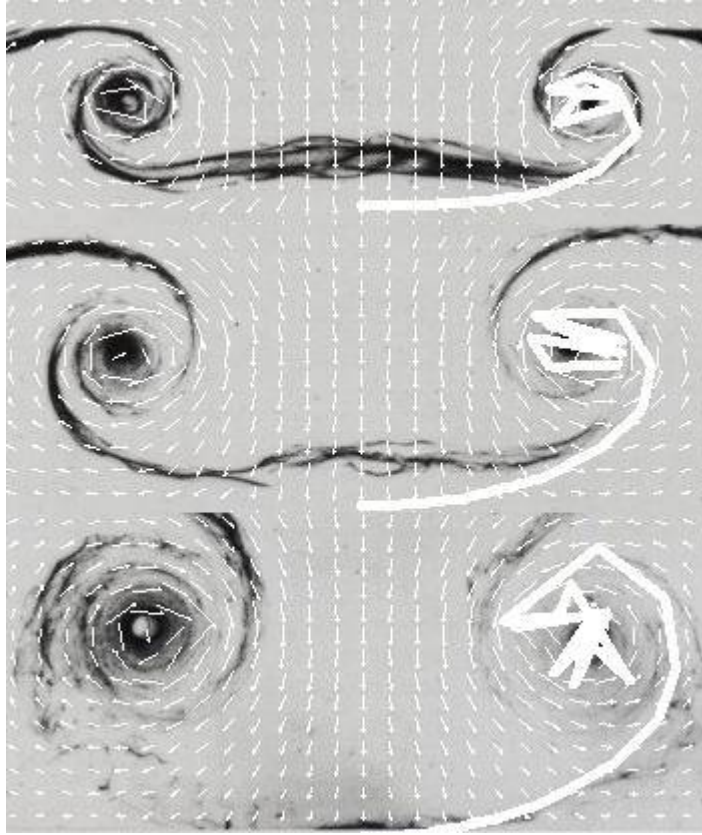
Figure 23: Computational and experimental[47] wake shapes of a rectangular wing with aspect ratio 2.4. The cross sections of the wake are 5.5, 11.2, and 21-chord lengths downstream of the trailing edge region.

In general, the theoretical and experimental shapes of the trailing shear layers agree well, especially in the locations of the rolled-up tip vortex. Differences exist, however, towards the center of the wing, most likely due to the flow being separated on the wing and the initially turbulent wake of the experiment. The turbulent wake and its finite thickness have lesser downwash effects than the theoretical wake model with zero thickness. This effect is more dominant along the centerline, where the thinning of the initially turbulent wake-

vortex sheet takes longer than near the tip vortices with its higher induced velocities. Consequently, experiment and theory agree better in that region.

As it can be observed in Fig. 23, the shear layer of the theoretical wake intersects with itself as it rolls-up into the tip-vortex. This behavior is not necessarily physical. In reality, the high velocity gradients and viscosity result in dissipation and a reduction of induced velocities in the vortex core. Nevertheless, even the irrotational model shows a reduction in induced velocities towards the center of the tip vortex, as becomes apparent from the overlaid crossflow velocity-vector field in Fig. 23. More importantly, the numerical solution is well behaved despite the self-intersection. This is an excellent example of the numerical robustness of the method using distributed vorticity elements, which allows the self-intersection of its potential flow solutions in the wake without singularity issues. This robustness is achieved without any violations of the irrotationality assumption of potential flow, as is the case, for example, with solid cores models.

4.7.2 Circulation Concentration in Tip Vortex

Another comparison of the distributed vorticity-element method with experimental results is shown in Fig. 24. In the wind-tunnel experiment, rotational speeds were measured with a vorticity meter in four transverse planes behind the 1/12-model of an L-19 wing.[48,49] In contrast to that, the computational results show contours of the crossflow velocities in the same four transverse planes that are 1, 2, 3 and 4 inch aft of the trailing edge. The root chord of the wing is 5.33 inch. For the computation, the wing geometry, the free-stream

velocity of 110 ft/sec, and the angle of attack of 12° are matched with the experiment. The theoretical model used 25 distributed vorticity elements along the halfspan.

The theoretical model predicts the location of the rolled up tip vortex quite well, although its exact position is difficult to determine. The agreement with the experiment exists despite the closeness to the trailing edge of less than a chord and, thus, the presence of lingering viscous effects in the wake of the experiment. Those effects are indicated by the significant rotational speed contours that were measured further inboard from the wingtip. They are caused by the shear layer coming off the trailing edge that is not rolled up in the tip vortex, yet. The locations of the shed shear layer of the experiment coincide with the locations of the vortex sheet of the theoretical prediction that are indicated with dash-dotted lines in Fig. 24.

The experimental and theoretical amounts of circulation that are concentrated in the rolled-up portions of the wakes agree reasonably well. According to Ref. 48, the circulation concentrated the tip vortices is approximately 18.4 ft^2/sec in the four transverse planes. The corresponding values of the theoretical model are determined by computing the contour integral of Eq. 1 along the 17.5 ft/sec contour lines. The subsequent results yield circulation values of 21.8, 19.1, 26.3, and 24.5 ft^2/sec in the four transverse planes that are 1, 2, 3, and 4 inch aft of the trailing edge, respectively. A more consistent agreement with the experiment is found for the 3 and 4 inch transverse planes if the integration path along the 17.5 ft/sec contour line is

63

modified along the thick, dashed lines in Fig. 24. In those cases, the circulation

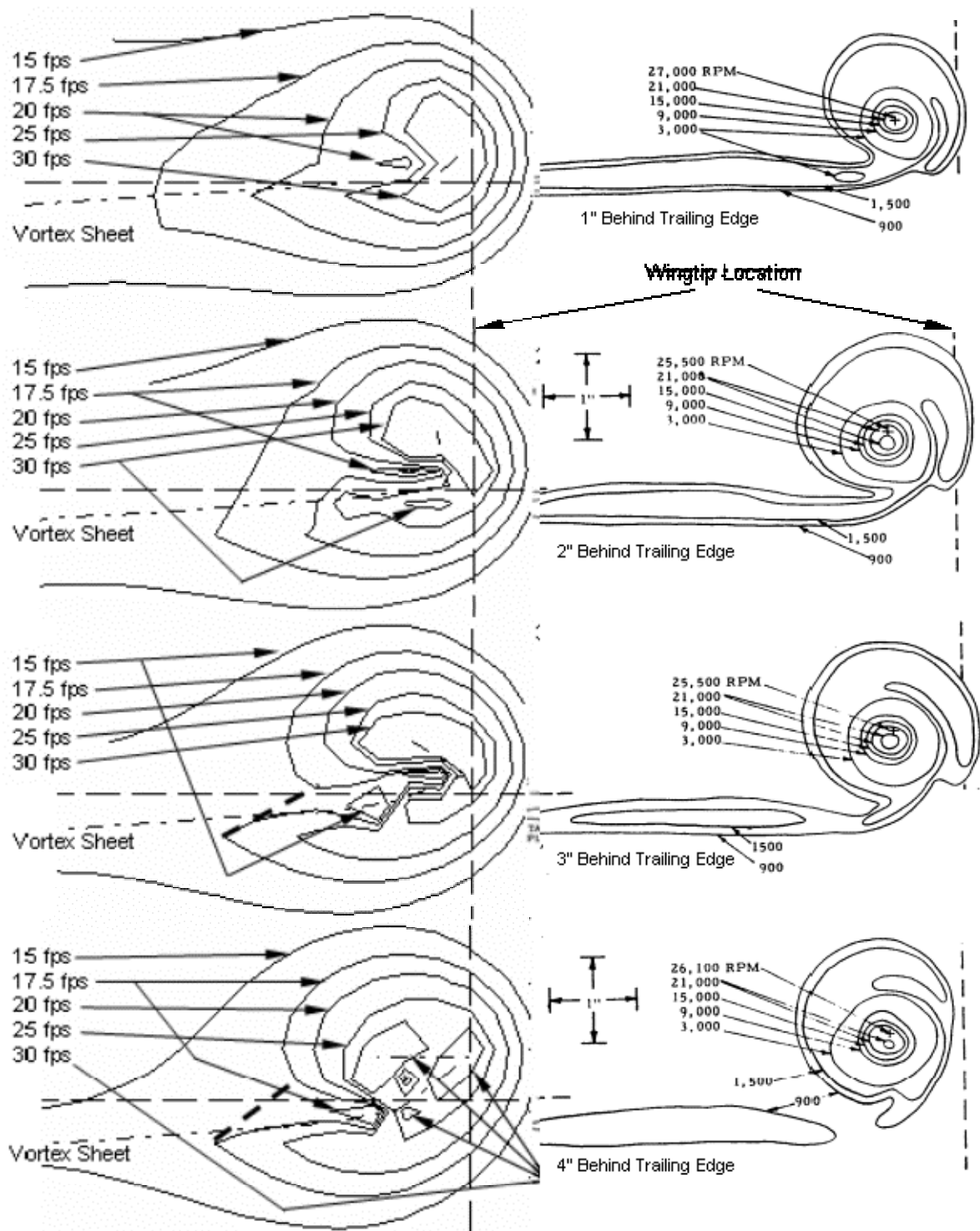values are 20.1 and 20.4 ft^2/sec, respectively.

Figure 24: Crossflow-velocity and constant rotational speed contours in four transverse planes behind the trailing edge of a 1/12-model L-19 wing. The crossflow velocities on the left are of computational origin using distributed vorticity elements, whereas the experimental data on the right were measured with a vorticity meter.[48,49]

4.7.3 Crossflow Velocities

A good quantitative measure of the force-free, potential-flow method that uses distributed vorticity element is given in Fig. 25. The figure shows the experimental[50] and theoretical crossflow velocity-vector fields that are located approximately two-wingtip chords, or approximately 32 inches, behind the trailing edge of a wind-tunnel model of a second-generation jet-transport wing having half span of 156 in. A top view of the wind-tunnel model is shown in Fig. 26. As part of an investigation of the effectiveness of winglets, crossflow velocity-vector fields were measured with a special wake rake. The computational wing model consists of one row of 40 distributed vorticity elements in the spanwise direction. The planform geometry and twist are the same as those of the original tests.

The two vector fields agree comparatively well in magnitude and direction. The major differences appear to be the locations of the centers of rotation and the shear-layers. The greatest differences exist near the centers of rotations, where the velocity gradients become large. Thus, small numerical errors and the influence of viscosity in the experiment dominate and can cause some deviations. To aid the comparison, the computed wake has been adjusted upwardly by 3.5 inches in Fig. 25. A plausible explanation for the small vertical offset of the wakes is that the wind-tunnel model wing bends approximately 1.5° under the aerodynamic loads, whereas the theoretical model remains rigid. Further inaccuracies are introduced by differences in the spanwise circulation distributions as well as in the streamwise location of the crossflow surveys.
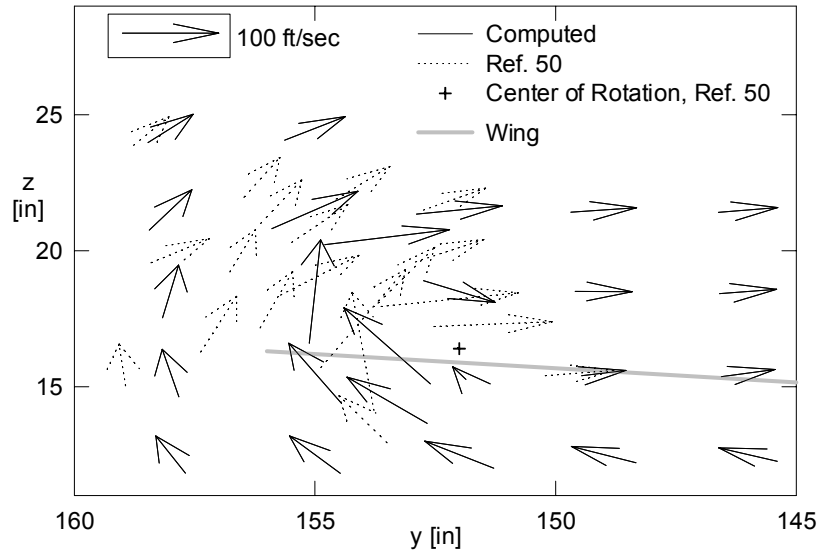
Figure 25: Computational and experimental[50] crossflow-velocity vectors approximately two-wingtip chords behind a second-generation jet-transport wing, $M_\infty = 0.700$, $C_L = 0.53$.
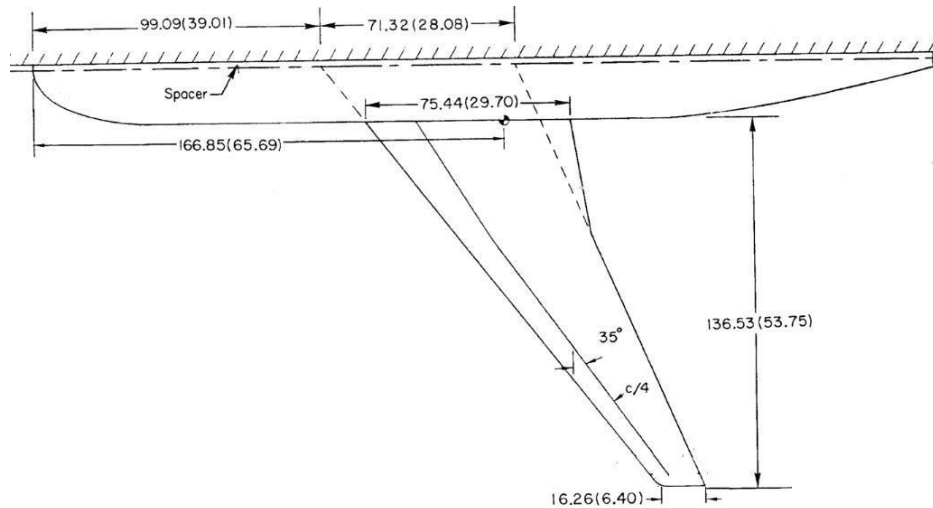
Figure 26: Top view of wind-tunnel model with a 156-in half-span that was used for crossflow measurements.[50] The experimental and computational surveys whose results are shown in Fig. 25, were performed approximately two wingtip chords or 32 inches behind the trailing edge in the wingtip region.

5   Sample Applications

In this section, several sample applications demonstrate the potential and numerical robustness of the relaxed wake method that uses distributed vorticity elements. In particular, the examples show the advantage of modeling wakes with vortex sheets that are allowed to rollup. Despite very strong interactions between different wakes and lifting surfaces, the numerical solutions are extremely well behaved.

5.1   Wing-Horizontal Tail Interactions

The higher-order lifting-surface method that uses distributed vorticity elements is used to investigate the wing-horizontal tail combination of a small, low-cost uninhabited aerial vehicle, or UAV. The UAV considered here is meant as a cost effective alternative for the inspection of pipelines or power lines. The aircraft has a maximum takeoff weight of 55 pounds, a range of 200NM, and cruises at approximately 50kt. In order to simplify transport and handling, the maximum dimension of the stowed aircraft is 5ft. For this purpose, the 8ft wing has 1.5ft wingtips that are foldable. Several wing-horizontal tail geometries are investigated for their induced drag at cruise and potential maximum lift for takeoff and landing.

Three wing-horizontal tail configurations were investigated. The basic two planforms are shown in Fig. 27. Wing 1 has a rectangular planform that was investigated with and without 3º washout. The second planform, wing 2, has three trapezoids per halfspan, with taper breaks at $y/b = 0.35$ and 0.475. Both

wing planforms have the same area as well span and, consequently, identical aspect ratios of 8. The horizontal-tail area is an eighth of the wing area and has an aspect ratio of 4. Its taper ratio is 1/3. All surfaces have straight trailing edges.

The computations were performed with 20 distributed elements across the halfspans of the main wings and five across the halfspan of the horizontal tail. Only one chordwise row was used. The streamwise step size in the wake was 0.025b. The convergence criterion for developing the wake was a change in span efficiency of less than 0.0001. In the case of the wing-horizontal tail combinations, the lift and induced drag forces were computed for each surface. In order to achieve longitudinal trim, the horizontal-tail incidence-angle was iteratively adjusted until the residual pitching moment was less than 0.005.
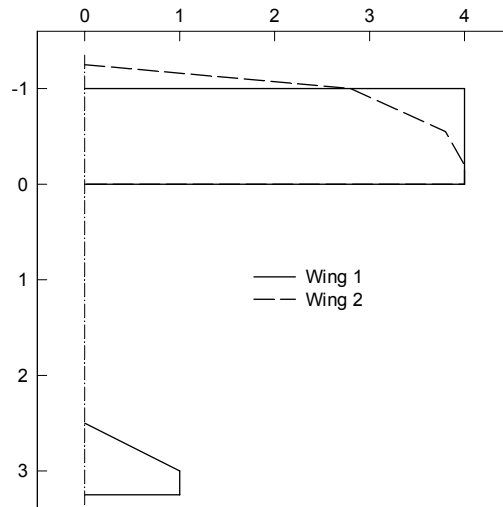
Figure 27: The planforms of the wing-horizontal tail geometries that were investigated. Wing 1 was examined with and without 3° washout. Wing 2 has no twist.

The span efficiencies of the individual lifting surfaces alone are plotted in Fig. 28. The three wing geometries, as well as the horizontal tail, have

efficiencies that are close to unity. Very obvious is the sharp drop-off in the span

efficiency that can be observed for wing 1 with washout at lift coefficients less

than 0.4. Wing 2 performs best with respect to its span-efficiency factor over the

investigated lift range.
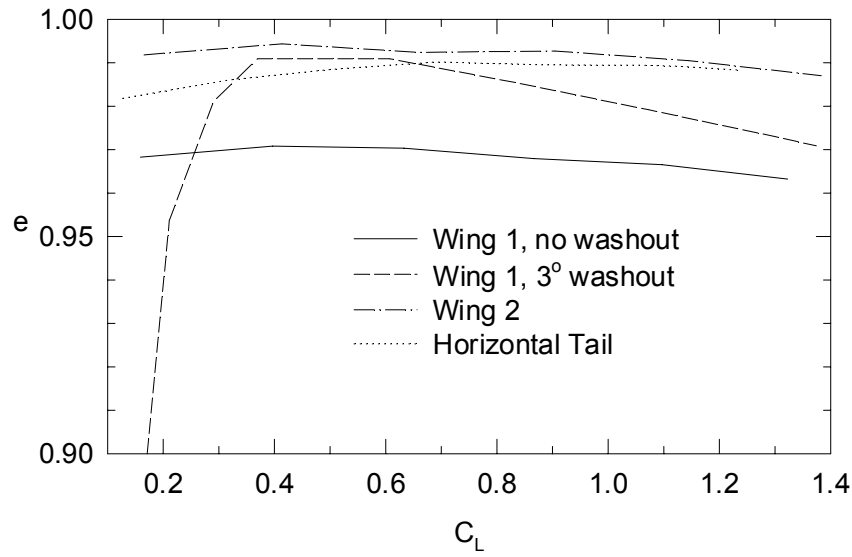
Figure 28: Span efficiency versus lift coefficient of the different surfaces alone.

The corresponding normalized spanwise circulation distributions are

plotted in Figs. 29 and 30 for the lift coefficients of cruise and high lift,

respectively. Also shown in both plots are elliptical distributions. Wing 1 with 3°

washout and wing 2 follow the elliptical distributions relatively closely. All three

versions exhibit an increased tip loading in comparison to the elliptical circulation
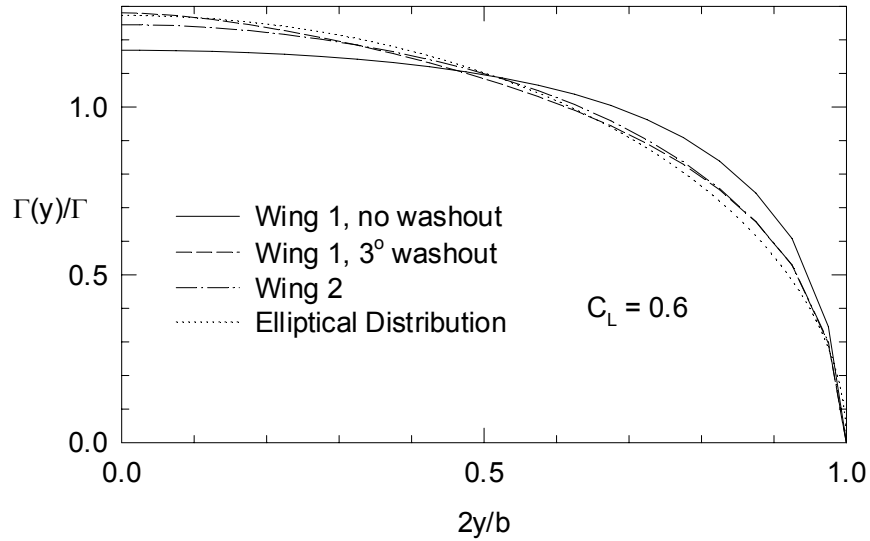
distribution.

Figure 29: The normalized, spanwise circulation distributions of the different wing geometries at the cruise-lift coefficient.
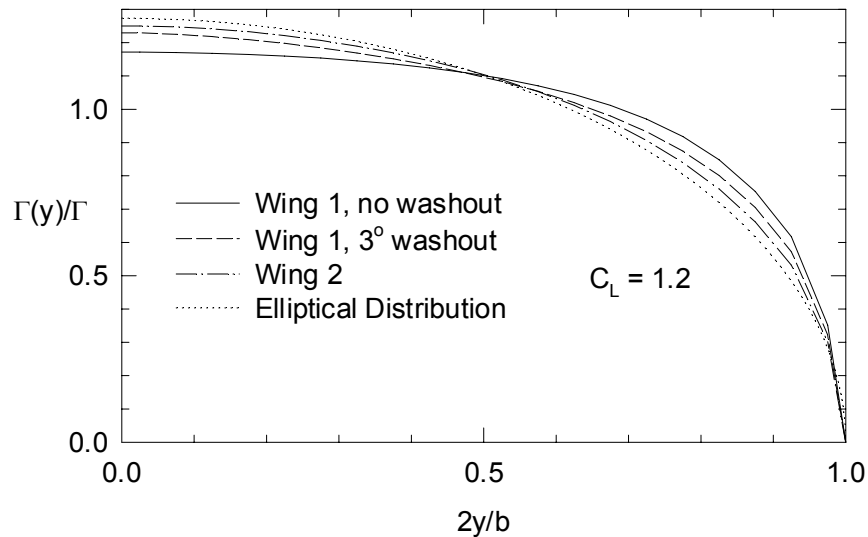
Figure 30: The normalized, spanwise circulation distributions of the different wing geometries at high lift.

At high angles of attack, the spanwise lift distribution is of great interest with regard to predicting the stall behavior of the wing. Due to the relatively low chord Reynolds numbers, that range from approximately 350,000 at slow speeds to roughly 500,000 at cruise, the maximum lift coefficient of the chosen airfoil is

71

limited to about $c_{l\,max} = 1.2$.[51] As shown in Fig. 31, approximately three-quarters of the span of wing 1 operates beyond that maximum lift coefficient, whereas wing 2 is largely within the limits. Thus, wing 2 has a lower stall speed or, alternatively, requires less wing area for the same stall speed as wing 1. The subsequent smaller wing area would have less cruise drag than the larger wing 1.
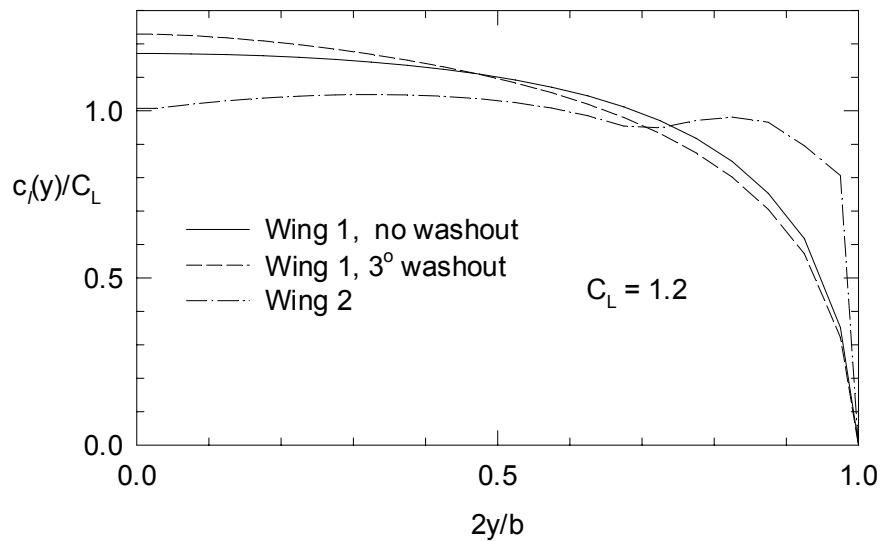
Figure 31: The normalized, spanwise lift distributions of the different wing geometries at high lift.

In order to assess their performances, each wing-horizontal tail configuration is trimmed for the different angles of attack by iteratively adjusting the horizontal tail-incidence angle until the longitudinal pitching moment is less than 0.005. Each configuration has a 10-percent static margin. The wings have zero-lift moment-coefficients of -0.1.

In this study, the neutral point location was determined by finding the center of gravity location with a zero di_{ht}/dC_L-derivative. This approach is very similar to what is done in flight test. It requires the determination of longitudinal

72

trim solutions of different center of gravity locations, as shown as an example in

Fig. 32 for the wing 1-horizontal tail configuration. In this figure, the horizontal-

tail incidence-angles for trim, i_{ht}, are plotted over the angle of attack range of

three different center of gravity positions. Unlike in flight test, the computational

approach safely allows center of gravity locations aft of the neutral point.

Subsequently, the zero-di_{ht}/dC_L derivative is determined through a simple

interpolation, as shown in Fig. 33, in which the horizontal-tail incidence-angle

derivatives are plotted for different centers of gravity. The neutral points of the

three configurations that were investigated in this study are located

approximately at the midchords of the wing roots.
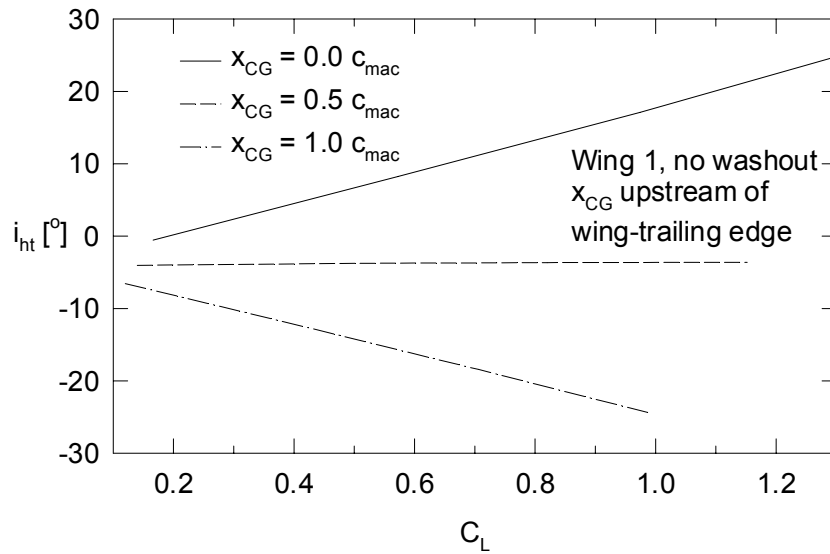
Figure 32: Horizontal-tail incidence-angles for trim at different lift coefficients and center-of-gravity locations of Wing 1 without washout.
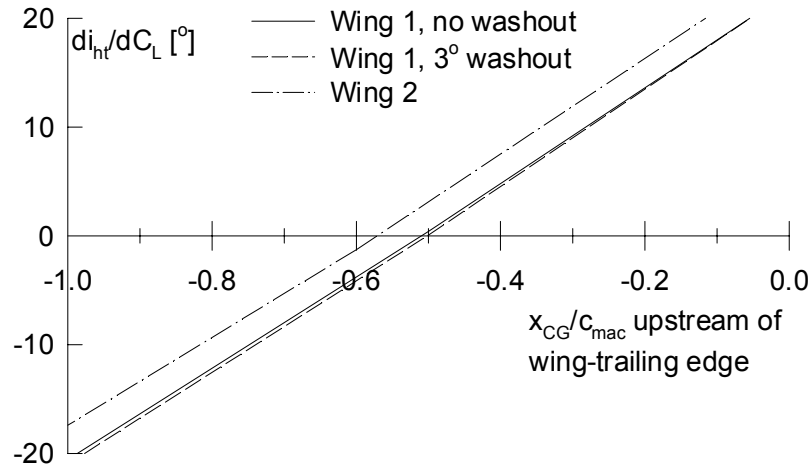
Figure 33: Horizontal-tail incident-derivatives at different center-of-gravity locations.

An example of the shape of the vortex sheets that are shed by the wing 2 and its horizontal tail is shown Fig. 34. The trailing edge of Wing 2 is located at the top of the figure. The figure does not depict any of the lifting surfaces and only the right half of the wake is shown. Clearly visible is the rollup of the waketip of the wing on the right of the figure. Furthermore, because of the download carried by the horizontal tail, its wake induces upwash, although it is relatively small. Thus, the horizontal tail-wake tip rolls downward. Despite the relatively small velocities induced by the tail, the main wake is deformed in this region, especially where the horizontal tail-tip wake interacts.
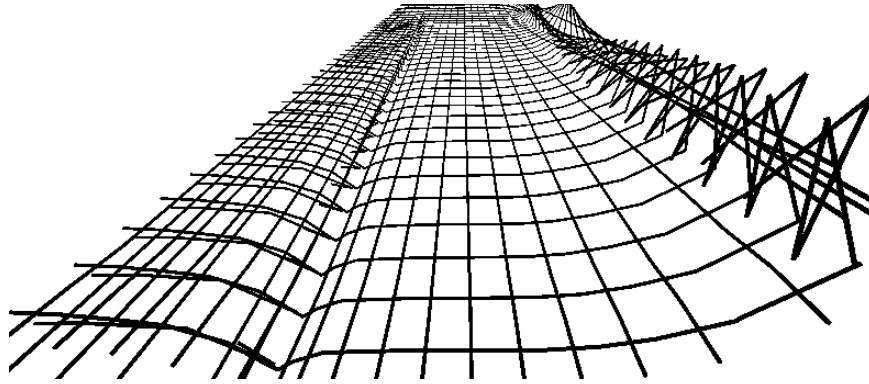
Figure 34: Looking upstream along the vortex sheets that are shed into the wake from Wing 2 and its horizontal tail under trimmed conditions at C_L = 0.6. The wing-trailing edge is at the top of the figure. The left edge of the vortex sheet that is depicted in the figure borders the symmetry plane of the wing-horizontal tail configuration.

The computed combined span efficiencies of the wing-horizontal-tail configurations are plotted in Fig. 35. The lift-coefficients of the horizontal tails that are required for trim at the corresponding lift coefficients are plotted in Fig. 36. The most significant result is the sharp drop-offs of the span efficiencies at the lower lift coefficients. Although the three wings have circulation distributions close the ideal one, as shown in Fig. 37 for a lift coefficient of 0.6, the relatively large downloads at the horizontal tails that are required for trim are detrimental to the overall efficiencies of the wing-horizontal tail configurations. In particular, the span efficiencies of wing 1 without twist and wing 2 suffer under the relatively large tail load at lift coefficients less than 0.5.

75
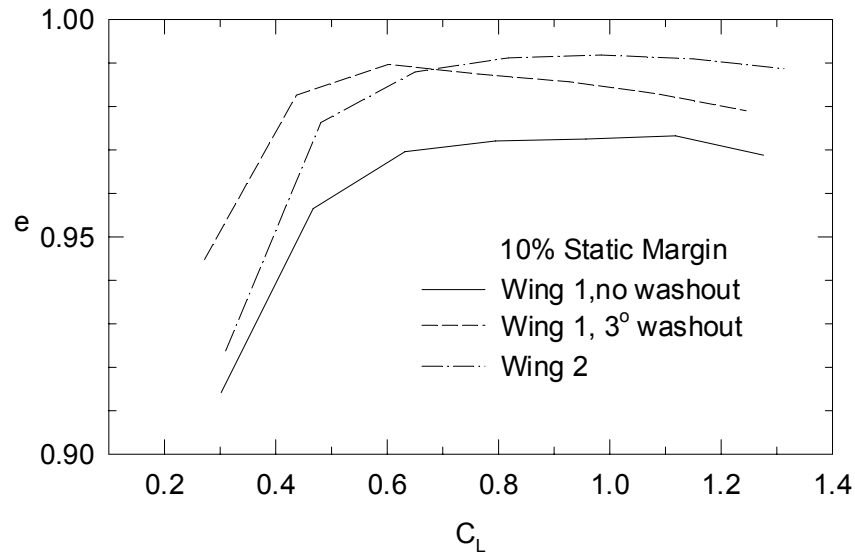
Figure 35: Span efficiency versus lift coefficient of the different wing-horizontal tail configurations.
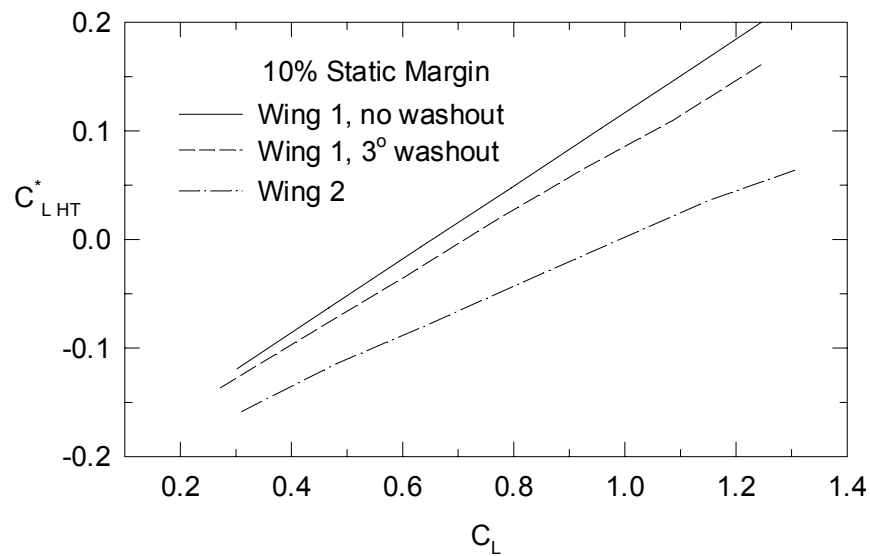
Figure 36: Horizontal-tail lift-coefficients required for trim of the three wing-horizontal tail configurations with 10%-static margin. The horizontal-tail coefficient is with respect to the tail-surface area.
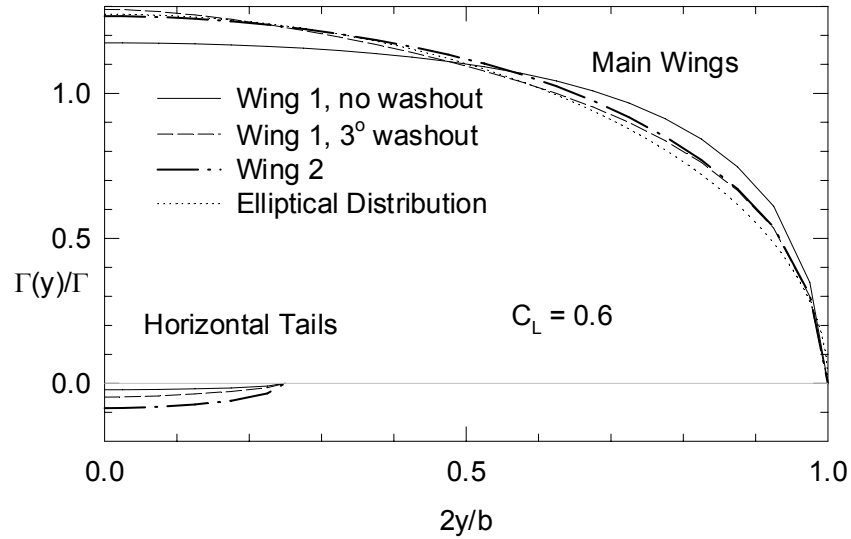
Figure 37: The normalized, spanwise circulation distributions of the different wing geometries at the cruise-lift coefficient.

The detrimental influence of the horizontal tail subsides at higher lift coefficients, as indicated in Fig. 35. At a lift coefficient of 0.8 and higher, the wing-horizontal tail configurations of wing 1 without twist and wing 2 perform as well as the wings independently, as observed by comparing the results presented in Fig. 35 with those of Fig. 28. The normalized spanwise circulation distributions that the different surfaces produce at a lift coefficient of 1.2 are plotted in Fig. 38. In the case of the wing 2 configuration, the high efficiency of the nearly elliptical circulation distribution of the main wing is largely undisturbed by the tail surface and its relatively small amount of circulation. The additional lift produced by the horizontal tails of the Wing 1 configurations, as shown in Fig. 39 for C_L=1.2, is relatively insignificant, especially when considering that the lift coefficients in this plot are with respect to their corresponding surface areas. Thus, they contribute only very little to the overall lift and cannot compensate for the loss in lift of the main wings that are possibly stalled for a large part.

77
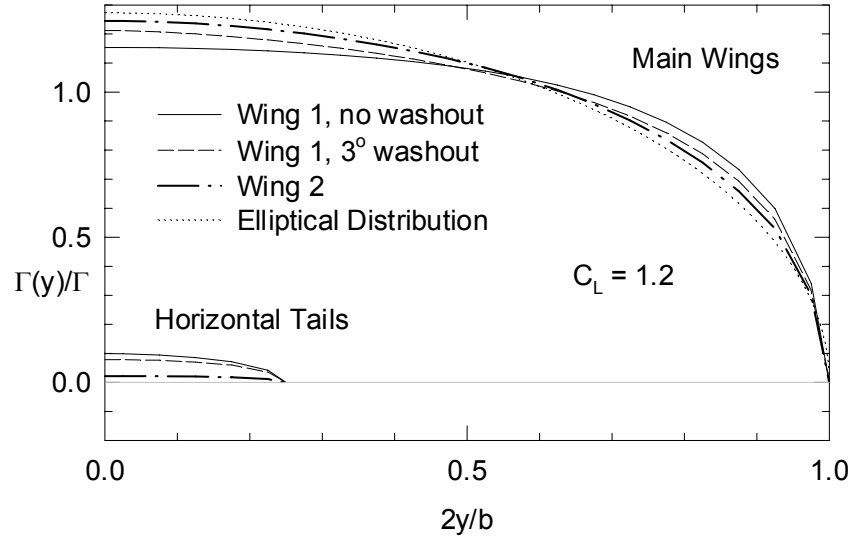
Figure 38: The normalized, spanwise circulation distributions of the different wing-horizontal tail configurations at high lift.
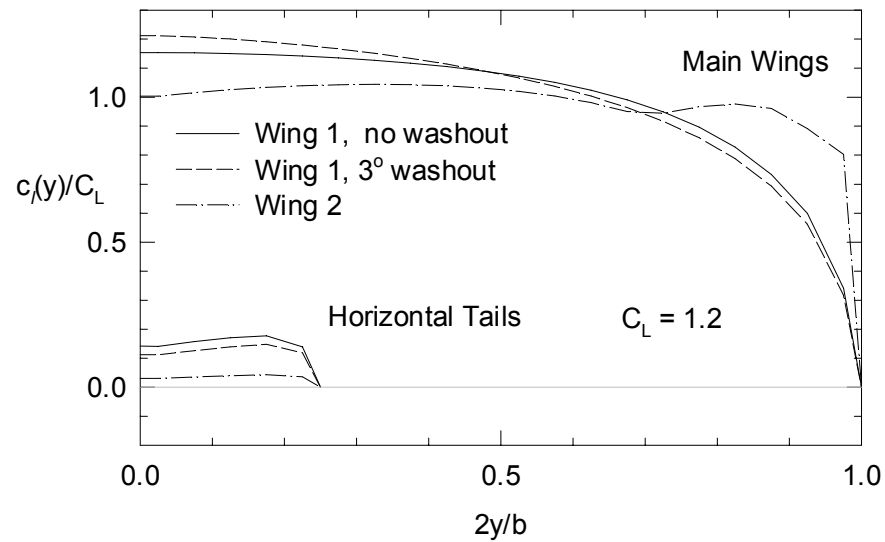
Figure 39: The normalized, spanwise lift distributions of the different wing-horizontal tail configurations at high lift.

In summary, of the configurations considered, wing 2 satisfies best the requirements for the UAV. As shown in Fig. 40, this wing planform has a high span efficiency at high lift coefficients, where induced drag is most significant. Only a moderate induced-drag penalty is paid at a cruise-lift coefficient of 0.6,

especially when considering that induced drag is proportional to the square of the lift coefficient. Beneficial of this wing planform is its efficient lift production at high lift. As is also apparent from Fig. 40, the use of the relaxed wake model has only a small influence on the computed span efficiencies of the wing-horizontal tail configurations. A fixed, drag free wake model underestimates the span-efficiency factor by roughly one percent.
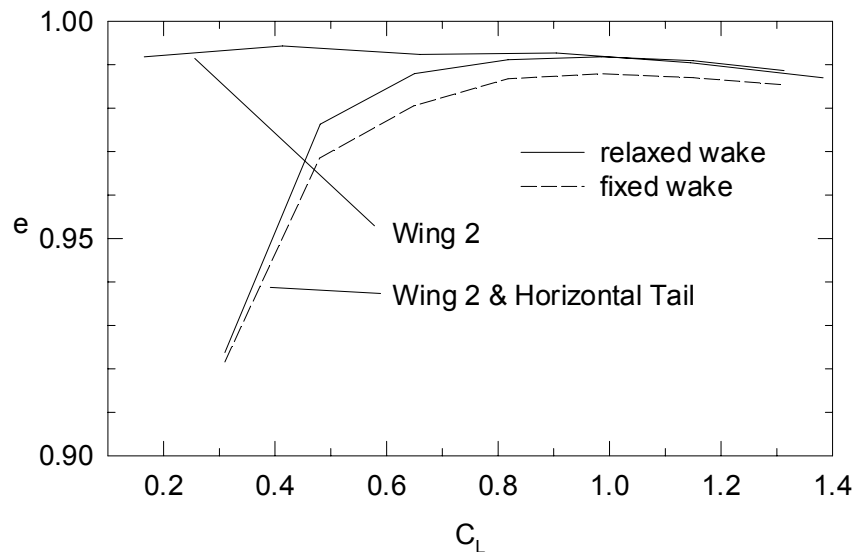
Figure 40: Span efficiencies of wing 2 with and without horizontal tail.

Independent of the wake model, the performance of wing 2 with a horizontal tail is considerably worse than that of the plain wing at lower lift coefficients, as it is apparent in Fig. 40. This loss in performance is primarily due to the penalty of trim drag. At the lower lift coefficient, the horizontal tail caries a considerable download, as it is visible in Fig. 41. Consequently, the main wing has to work harder and the overall induced drag performance of the configuration suffers. Possible ways to reduce this degradation at low lift coefficients are either a reduction of the zero-lift pitching moment of the wing with a trailing edge

flap that is deflected upward, or with a more aft location of the center of gravity. The latter is, however, limited by the flight control system, whereas the former might carry a profile-drag penalty, especially at higher flight speeds.
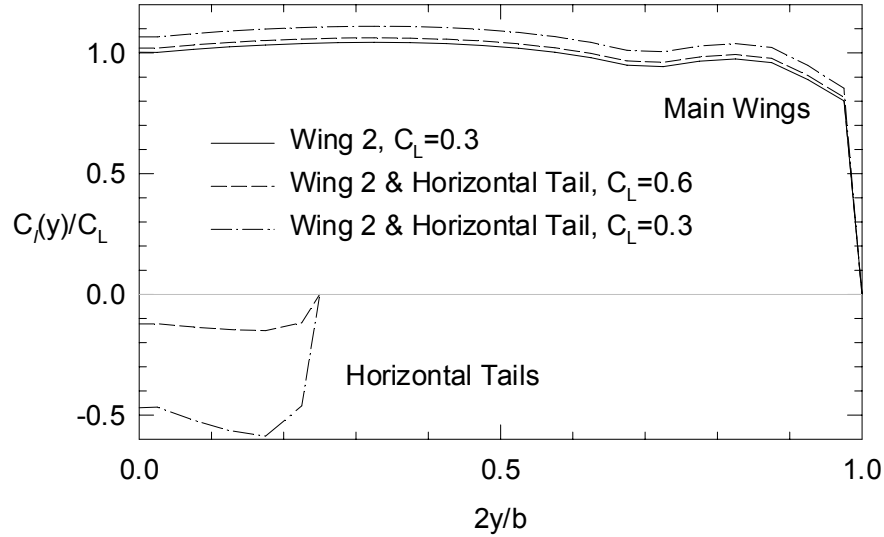
Figure 41: The normalized, spanwise lift distributions of the wing 2 with and without a horizontal tail at lower lift coefficients.

5.2   Formation Flight

Formation flight can increase the span efficiency of a system of flight vehicle considerably.[52] As migrating birds demonstrate on a regular basis, a significant amount of effort can be saved by flying in the upwash field that exists beyond the rolled up tip vortices of a leading aircraft or bird. Such upwash fields are visible in Figs. 23 and 25. Ultimately, the upwash tilts the lift vector of the follower forward and, thus, reduces its induced drag. The induced drag reduction, however, is not limited to the follower, since the leader is similarly subjected to the upwash field that the bound circulation of the follower produces.

Obviously, this effect is less pronounced and decreases quickly with increasing streamwise spacing in the formation.

Especially with regard commercial aviation, formation flight has the potential of improving the span efficiencies without the structural and aeroelastic issues that usually accompany high aspect-ration wings. With modern flight-control systems a close enough, but safe, spacing has become feasible in order to realize the performance benefits of formation flight.

Modern competition sailplanes commonly make use of the advantages of formation flight. Besides extending their gliding range, formation flight helps in the detection of thermals. An example of such a formation is shown in Fig. 42, with two Standard Cirrus sailplanes.

A formation of two such sailplanes was investigated using the relaxed wake method with its distributed vorticity elements. The wing of the Standard Cirrus has a span of 15 meters and an aspect ratio of 21.9. Its wing has 3º dihedral, and the planform consists of two trapezoids per halfspan with taper breaks at about 60-percent of the halfspan. The outer wing panel has 1.5º washout. The formations investigated were separated by half a span in streamwise direction. Several lateral separations were assessed at a lift coefficient of approximately 0.58, which is slightly less than the lift coefficient of the best lift-to-drag ratio. The lateral separations that were considered ranged from the aircraft centerlines being inline to being 1.2 spans apart. The vertical spacing was zero. Each aircraft wing was modeled with 20 distributed elements in the spanwise and one in the chordwise directions. In the wake, the

streamwise length of the distributed vorticity elements was 2.7-percent of the span.

Figure 42: Two Standard Cirrus sailplanes in formation flight.

In the case of a lateral offset in the formation, both aircraft must be trimmed for roll. Primarily, the wake of the lead aircraft interacts with the lifting surface of the follower, although the follower aircraft, especially its bound vorticity, has a limited impact on the lift distribution of the lead aircraft. Obviously, the latter interaction diminishes quickly with increasing streamwise distance between the aircraft. The rolling moments are adjusted by changing the incidence angles of the outer wing panels, in the present case, using the outer 40-percent of the span, which corresponds with the location of the ailerons. Similar to an aileron deflection, the incidence angles are adjusted in opposite directions on the left and right outer panels. In addition to roll, the pitch attitude of the follower aircraft must be adjusted in order to match the speeds of the two aircraft. Thus, three separate iteration loops are required to obtain a converged wake shape, zero rolling moment, and matched lift coefficients.

The computed span efficiencies of the formations with varying spanwise stagger are plotted in Fig. 43. Shown are the span efficiencies of each wing and of the combined formation. The combined value is not necessarily the simple average of the two single span efficiencies, rather, when both aircraft operate at the same lift coefficients and have equal wing areas, the total efficiency of the formation is related to the single efficiencies of each aircraft by:

$$e_{formation} = \frac{C_{L\,formation}^2}{\pi A C_{Di\,formation}} = \frac{\left(C_{L\,leader} \dfrac{S_{leader}}{2S} + C_{L\,follower} \dfrac{S_{follower}}{2S} \right)^2}{\pi AR \left(C_{Di\,leader} \dfrac{S_{leader}}{2S} + C_{Di\,follower} \dfrac{S_{follower}}{2S} \right)}$$

(13)

$$e_{formation} = 2 \frac{e_{leader}\, e_{follower}}{e_{leader} + e_{follower}}$$

As expected, the formation has its worst performance when the following aircraft is directly in the wake of the leader. Even the lead aircraft performance suffers slightly with a span efficiency of 0.88 in comparison to nearly one of a single aircraft. The follower-aircraft span efficiency is 0.37. This value improves considerably as the aircraft start to move apart in the spanwise direction. Even the lead aircraft performance improves slightly as both aircraft move apart. Primarily, however, the follower aircraft benefits from the performance gains. When the aircraft are spaced laterally by one span, the follower span efficiency becomes nearly twice as good as that of the base wing alone. A further increase in spanwise spacing reduces the gains in span efficiency.
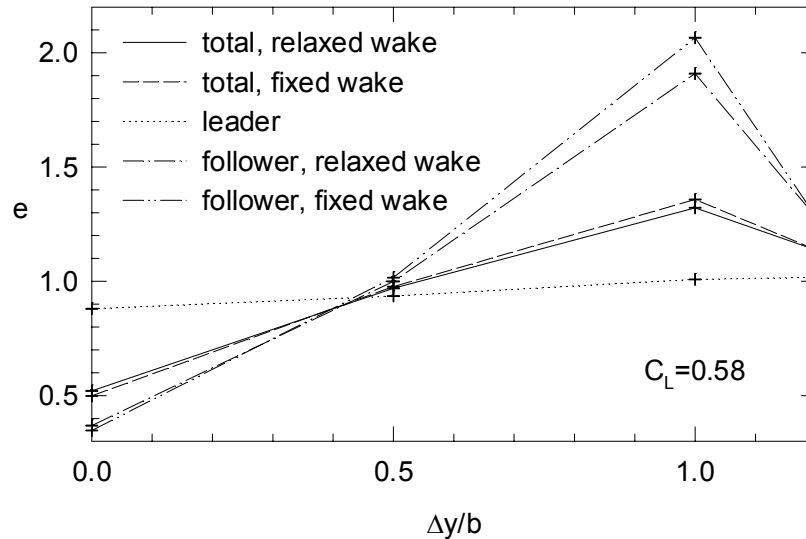
Figure 43: The span efficiency of a formation of two Standard Cirrus sailplanes that are half a span apart in streamwise direction with different lateral spacings.

The largest differences due to the wake model exist when the tip regions of the wakes interact, as shown in Fig. 44. This figure shows the shapes of the computed, free vortex sheets that are shed by the two-wing formation with a lateral spacing of $\Delta y = b$. Although the computed performance of the lead aircraft does not depend significantly on the wake model, the span efficiency of the follower aircraft exhibits some differences, as presented in Fig. 43. The fixed, drag-free wake model results in an approximately 7.5-percent higher span efficiency than is predicted using the free wake model. A further notable difference between the results of the two wake-models can be observed in Fig. 43 for the case of the aircraft centerlines being aligned. The fixed, drag-free wake model slightly underestimates the span efficiency. On the other hand, cases having a large overlap do not necessarily result in significant differences in predicted efficiencies, despite the strong interaction between the vortex sheets. The shapes of the computed, free vortex sheets of such the formation with a

84

lateral spacing of Δy=b/2 is shown in Fig. 45. Despite the obvious strong

interaction, the span efficiencies of both wake models are essentially equal in

Fig. 43.
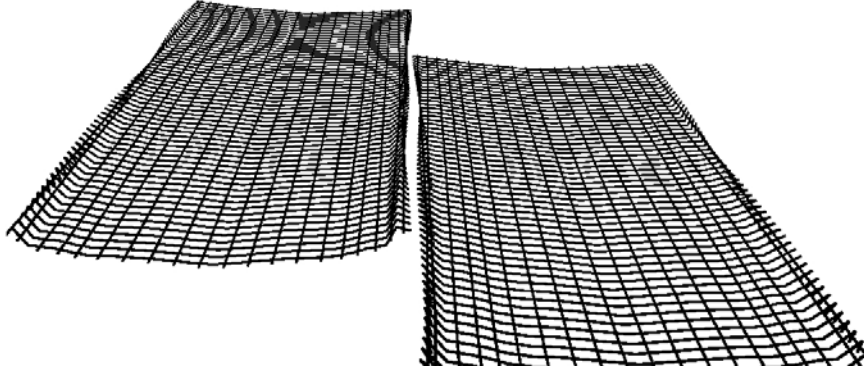
Figure 44: Looking upstream along the vortex sheets that are shed by the wings
of a two Standard Cirrus sailplanes that are flying in formation with a lateral
spacing of Δy=b. The trailing edges of the wings, which are not shown in the
figure, are located at the top of the figure.
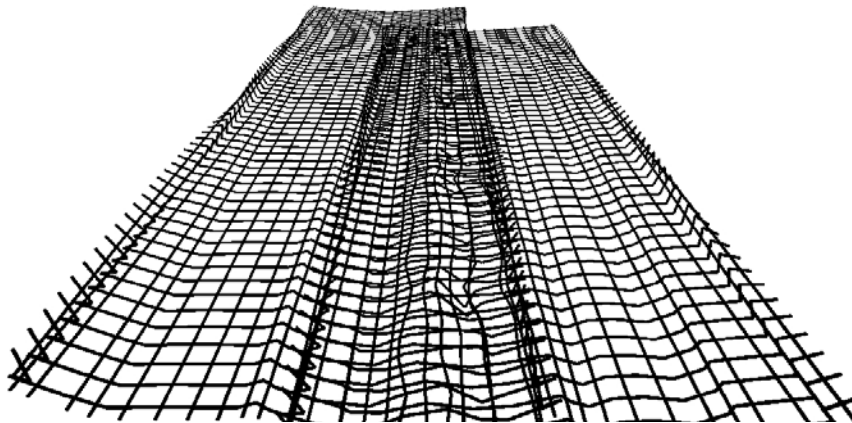
Figure 45: Looking upstream along the vortex sheets that are shed by the wings
of a two Standard Cirrus sailplanes that are flying in formation with a lateral
spacing of Δy=b/2. The trailing edges of the wings, which are not shown in the
figure, are located at the top of the figure.

The span efficiency of the follower aircraft in the formation with a lateral

spacing of Δy=b/2 is greatly compromised by the control inputs that are needed

to compensate for the rolling moment resulting from the interaction with the lead aircraft wake. The required control inputs are plotted in Fig. 46 for the different lateral spacings. The predicted control inputs are essentially identical for the fixed and relaxed wake models. The pitch adjustment in order to match the lift coefficients of both aircraft is relatively small. The exception is the case without any lateral spacing, when the follower aircraft has to increase its pitch attitude by almost 1° in order to compensate for the downwash that the lead aircraft wake induces. As expected, the roll corrections required by the lead aircraft are small. The lead aircraft of the $\Delta y=b/2$ formation, however, requires a small amount "right aileron" or $\Delta i_{tip}=0.05°$ in order to compensate for the upwash field that the bound vorticity of the follower aircraft induces on the lead aircraft right wing. In contrast to that, the follower aircraft in the same formation has to adjust its outer 40-percent span with a differential incidence angle of $\Delta i_{tip}=1.17°$. This corresponds to the amount of "right aileron" that is needed to compensate for the flow field that the wake of the lead aircraft induces onto the follower. The "aileron" correction is greatly reduced and reversed as the lateral spacing is increased.
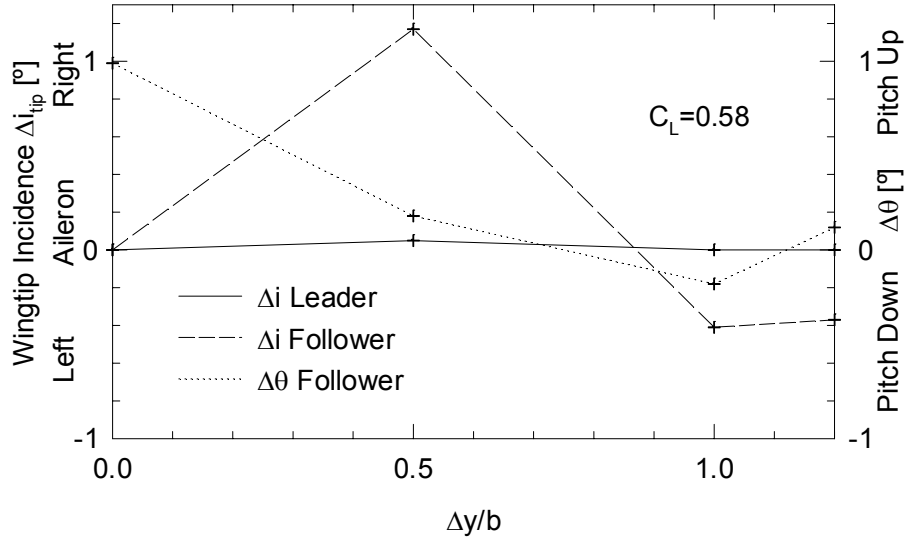
Figure 46: The required control inputs for trimmed flight of a formation of two Standard Cirrus sailplanes with different spanwise staggers and that are half a span apart in streamwise direction.

The detrimental effect of the relatively large roll correction of the follower aircraft of the $\Delta y = b/2$ formation also becomes apparent in the spanwise circulation distribution that is plotted in Fig. 47. This figure shows the normalized spanwise circulation distribution of the base wing alone, as well as those of the follower aircraft that are in formations with lateral spacings of half a span and one span. The large changes in spanwise circulation distribution of the $\Delta y = b/2$-formation results in a relatively large induced drag penalty that offsets any possible gains of this formation, as is indicated in Fig. 43. Additionally, the spanwise variation of the induced drag results in an adverse yawing moment because of the spanwise variation of the induced drag. Although not considered in the results that are discussed here, the rudder input for compensating the adverse yaw would result in additional drag and compound the performance penalty.

87

In contrast to that, the follower aircraft of the formation with a lateral spacing of Δy=b benefits from the upwash field of the lead aircraft wake without the need of any large aileron inputs, as apparent in Fig. 46. Thus, its adverse yaw penalty should be much smaller as well, as is suggested by its spanwise lift distribution in Fig. 47. The spanwise lift distribution is indeed relatively close to that of the base wing. In addition to the greater performance gain, the larger spacing of this formation ensures a safer operation than the closer formation would.
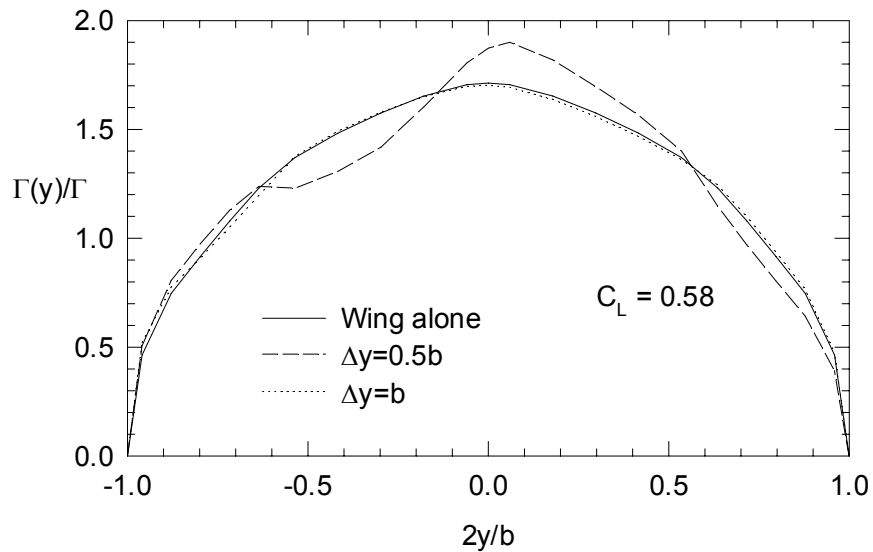
Figure 47: The normalized, spanwise circulation distributions of the following aircraft of a two aircraft configuration with varying lateral spacing.

6   Conclusion

A higher-order, lifting-surface method is introduced that uses elements with distributed vorticity in order to model lifting surfaces as well as the vorticity that is shed into the wake. One or several spanwise systems consisting of such elements are used to model the lifting surface. The elements are placed along the zero-lift plane of the wing, thus essentially making this a vortex-lattice method. In the wake, the distributed vorticity elements are displaced with the local flow field in order to realize a force-free wake. The induced drag is computed along the trailing of the lifting surfaces by applying the Kutta-Joukowsky theorem using the velocity induced there by the wake and the vorticity that is shed from the wing at this location.

The new method shows good agreement with the elliptical-loaded wing results of the classical lifting-line theory. Likewise, good agreement exists when results of the method are compared with those of other theoretical methods. In addition, this agreement is reached using considerably fewer panels than the other methods considered. In particular, the drag computation along the trailing edge is less sensitive to paneling-density variations of the lifting surface and in the wake. The most apparent advantage of the reduced number of panels required is an increase in computational speed.

In comparison with experimental results, the newly developed method yields similar flow fields in the wake of a wing. It identifies correctly the location of the tip vortex and of the shear layer behind the wing-trailing edge. Besides the qualitative assessments, the method predicts the amount of circulation that is

concentrated in the tip vortex well, and also yields very good agreement with the experiment when comparing the actual crossflow-velocity vector fields in the wake.

Besides its accuracy, the biggest advantage of the new method over other potential flow methods is its numerical robustness despite the free-force wake model. The relaxed wake that is modeled as a vortex sheet rolls up without any of the erratic behavior common to many other singularity methods. Simultaneously, the numerical stability is achieved without compromising the potential flow assumptions, as, for example, it is the case with models that use vortices with solid cores. Thus, even multiple wing systems can be modeled easily and correctly, since the distributed vorticity elements induce finite velocities throughout the entire wake. Consequently, the rollup is extremely stable, even when the wake-vortex sheet intersects itself and an increasing amount of it becomes concentrated in the tip-vortex region.

Overall, the numerical accuracy and stability of this method make it suitable for applications with strong interactions between the lifting surfaces and their subsequent wakes. Because the method is capable of modeling wakes for long distances downstream without problems with singularities, it is well suited for the adaptation to the modeling of wake interactions with regard to helicopter rotors. Thus, it could be useful for dealing with rotorcraft issues, such as blade-vortex interactions and vibratory loadings. Likewise, its extension to a panel method that models the thickness of the wing is desirable. In order to streamline the computational effort, it might be possible to modify the induced drag

computation. This modification would take advantage of the Kutta condition that has to be satisfied along the trailing edge and, thus, determines the bound vorticity. The Kutta condition might allow the substitution of the velocities that the wake elements induce along the trailing edge with a combination of the free-stream velocity and the velocities induced by the surface elements. Consequently, the computational speed could be further improved, since there are generally fewer surface than wake elements.

References

1   Prandtl, L.,"Tragflügeltheorie," Göttinger Nachrichten, *Mathematisch-Physikalische Klasse*, Germany, 1918, pp. 451-477.

2   Prandtl, L.,"Application of Modern Hydrodynamics to Aerodynamics," NACA Report 116, 1921.

3   Lanchester, F.W., *Aerial Flight*, Constable, London, England, 1907.

4   Maughmer, M.D., "About Winglets," *Soaring*, June 2002, pp. 18-23 .

5   NASA Langley Research Center, 1990 ID EL-1996-00130.

6   Kroo, I., Wakayama, S., "Nonlinear Aerodynamics and the Design of Wing Tips," NASA CR-190649, April 1992.

7   Thomas F., *Fundamentals of Sailplane Design,* Judah Milgram, translator and contributor, College Park Press, College Park, Maryland, 1999.

8   Johnson, W., *Helicopter Theory*, Dover Publication, New York, 1994.

9   Hinton, D.A., "Aircraft Vortex Spacing System (AVOSS) Conceptual Design," NASA TM-110184, August 1995.

10   Betz, A., "Ein einfacher Beweis des Munk'schen Satzes," *Jahrbuch der Wissenschaftlichen Gesellschaft für Luftfahrt*, Vol 5, Anhang 4, 1920, pp. 37-65.

11   Trefftz, E., "Prandtlsche Tragflächen- und Propeller Theorie," *Zeitschrift für Angewandte Mathematik und Mechanik*, 1921, pp. 206-218.

12   Munk, M.M., "Minimum Induced Drag of Aerofoils," NACA Technical Report No. 121, 1921.

13 Weissinger, J., "Über die Erweiterung der Prandtl'schen Teheorie der tragenden Linie," *Mathematische Nachrichten*, Berlin, Germany, 1949, pp. 45-106.

14 Weissinger, J., "The Lift Distribution of Swept-Back Wings," NACA TM-1120, 1947.

15 Hess, J.L. and Smith, A.M.O., "Calculation of Nonlifting Potential Flow about Arbitrary Three-Dimensional Bodies," Douglas Aircraft Rep. No. E.S. 40622, 1962.

16 Woodward, F.A., "Analysis and Design of Wing-Body Combinations at Subsonic and Supersonic Speeds," *Journal of Aircraft*, Vol. 5, No. 6, Nov.-Dec. 1968, pp. 528-584.

17 Katz, J. and Plotkin, A., *Low-Speed Aerodynamics*, McGraw-Hill, New York, 1991.

18 Kaden, H., "Aufwicklung einer unstabilen Unstetigkeitsfäche," Ing. Archiv, Vol. 2, May 1931, pp. 140-168 (English translation, R.A.E. Library Trans. 403.).

19 Krasny, R., "Computation of Vortex Sheet Roll-up in the Trefftz Plane," J. Fluid Mch., Vol. 184, 1987, pp. 123-155.

20 Rom, J., *High Angle of Attack Aerodynamics*, Springer-Verlag, New York, 1992.

21 Portnoy, H., "Thick, two-dimensional wake roll-up behind a wing of finite span-extended calculations," *Aeronautical Journal*, October 1977, pp. 460-463.

22 Lamb, H., *Hydrodynamics*, Dover, 6th ed., 1945.

23 Yeh, D.T., "Vortex Panel Calculation of Wake Rollup behind a Large Aspect Ratio Wing," Master of Science Thesis, University of Maryland, MD, 1985.

24 Nagati, M.G., Iverson, J.D., and Vogel, J.M., " Vortex Sheet Modeling with Curved Higher-Order Panels," *Journal of Aircraft*, Vol. 24, November 1987, pp. 776-781.

25 Milne-Thomson, L. M., *Theoretical Aerodynamics*, Dover Publications, New York, 1973.

26 Schlichting, H. and Truckenbrodt, E., *Aerodynamik des Flugzeuges Zweiter Band*, Springer-Verlag, Berlin, Germany, 1969.

27 Schlichting, H., and Truckenbrodt, E., *Aerodynamic of the Airplane*, McGraw-Hill, New York, 1979.

28 Horstmann, K.H., "Ein Mehrfach-Traglinienverfahren und seine Verwendung für Entwurf und Nachrechnung nichtplanarer Flügelanordnungen," Dissertation, DVFLR, Institut für Entwurfsaerodynamik, Braunschweig, Germany, DFVLR-FB 87-51, 1987.

29 Schlichting, H. and Kahlert, W., "Calculation of Lift Distribution of Swept Wings," RAE Rep. Aero. 2297, 1948.

30 Holme, O., "On the Approximate Solution of the Lifting Surface Problem with the Aid of Discrete Vortices," KTH-Aero TN 6, Stockholm, 1949.

31 Multhopp, J.H., "Methods for Calculating the Lift Distribution of Wings (Subsonic Lifting-Surface Theory)," ARC RM 2884, 1955.

32 Truckenbrodt, E., "Tragflächentheorie bei inkompressibler Strömung," *Jb. WGL*, 1953, pp 40-65.

33 Blenk, H., "Der eindecker als tragende Wirbelfläche," Dissertation, University Göttingen, Germany, 1923.

34 Blenk, H., "The Monoplane as a Lifting Vortex Surface," NACA TM-1111, 1947.

35 Maughmer, M.D., "The Design of Winglets for High-Performance Sailplanes," *Journal of Aircraft*, Vol. 40, No. 6, Nov.-Dec. 2003, pp. 1099-1106.

36 Kunz, P.J., "Development of a Software Package for the Assessment of High-Performance Sailplanes," Master of Science Thesis, The Pennsylvania State University, University Park, PA, 1997.

37 Schmid-Göller, S., "Zur genauen Berechnung des induzierten Widerstands von Tragflügeln," Doctoral Dissertation, Institut A für Mechanik, Universität Stuttgart, Stuttgart, Germnay, Oct. 1992.

38 Eppler, R., "Die Enwicklung der Tragflügeltheorie," 30. Ludwig-Prandtl-Gedächtnisvorlesung, *Z. Flugwissenschaft*, Vol. 11, Stuttgart, April 1987, pp.133-144.

39 Eppler, R., "Induced Drag and Winglets," *Aerospace Science and Technology*, No. 1, pp. 3-15, 1997.

40 Mortara, K.W. and Maughmer, M.D., "A Method for the Prediction of Induced Drag for Planar and Non-Planar Wings," AIAA Paper 93-3420-CP, August 1993.

41 Leyser, J., "Accurate Computation of Lift and Induced Drag at Lifting Surfaces," AIAA-96-2405-CP, June 1996.

42 Miranda, L.R., Elliot, R.D., Baker, W.M., "A Generalized Vortex Lattice Method for Subsonic and Supersonic Flow Applications," NASA CR-2865, 1977.

43 Eppler R. and Schmidt-Göller, S., "A Method to Calculate the Influence of Vortex Roll-up on the Induced Drag of Wings," Notes on Numerical Fluid Mechanics, Volume 25, *Finite Approximations in Fluid Mechanics II*, DFG Priority Research Programme Results 1986-1988, Vieweg Sohn, Braunschweig/Wiesbaden, Germany, 1989, pp. 93-107.

44 Smith, S.C. and Kroo, I., "Computation of Induced Drag for Elliptical and Crescent-Shaped Wings," *Journal of Aircraft*, Vol. 30, No. 4, July-August 1993, pp. 446-452.

45 DeHaan, M.A., "Induced Drag of Wings with Highly Swept and Tapered Wing Tips," AIAA Paper 90-3062-CP, Aug. 1990

46 Bippes, H., "Experimente zur Entwicklung der freien Wirbel hinter einem Rechteckflügel," *Acta Mechanica 26*, Springer Verlag, 1977, pp. 223-245.

47 Van Dyke, M. (Editor), *Album of Fluid Motion*, Parabolic Press, Stanford, 1982, p. 50.

48 Tangler, J.L., "A Study of the Vortex Sheet Immediately Behind an Aircraft Wing," Mater of Science Thesis, The Pennsylvania State University, University Park, PA, 1966.

49 McCormick, B.W., Tangler, J.L., and Sherrieb, H.E., "Structure of Trailing Vortices," *Journal of Aircraft*, Vol. 5, No. 3, May-June 1968, pp. 260-267.

50 Flechner, S.G., Jacobs, P.F., and Whitcomb, R.T., "A High Subsonic Wing-Tunnel Investigation of Winglets on a Representative Second-Generation Jet Transport Wing," NASA TN D-8264, July 1976.

51 Simons, M., *Model Aircraft Aerodynamics Fourth Edition*, Special Interest Model Books Ltd., Dorset, Great Britain, 1999.

52 Maskew, B., "Formation Flying Benefits Based on Vortex Lattice Calculations," NASA CR-151974, May 1977

Appendix 1: Induced Velocities of a Vortex Filament with a Parabolic Circulation Distribution

The solution of the integral of Eq. 5 yields the velocity at a point that is induced by a vortex filament having a parabolic circulation distribution in spanwise direction, $\Gamma = A + B\eta + C\eta^2$. As described in Ref. 28, the analytical integration can be written in the following way:

$$\underline{w}_1(\xi_0, \eta_0, \zeta_0) = \frac{1}{4\pi} \begin{bmatrix} Aa_{1\xi} + Bb_{1\xi} + Cc_{1\xi} \\ Aa_{1\eta} + Bb_{1\eta} + Cc_{1\eta} \\ Aa_{1\zeta} + Bb_{1\zeta} + Cc_{1\zeta} \end{bmatrix} \tag{A1-1}$$

Point $P_0(\xi_0, \eta_0, \zeta_0)$ is expressed with respect to the local reference frame of the vortex filament as indicated in Fig. A1-1.

In accordance with Ref. 28, the coefficients in Eq. A1-1 are computed using the following relationships:

$$\begin{array}{lll}
a_{1\xi} = -G_{11}\zeta_0 & b_{1\xi} = -G_{12}\zeta_0 & c_{1\xi} = -G_{13}\zeta_0 \\
a_{1\eta} = G_{11}\zeta_0 \tan\varphi & b_{1\eta} = G_{12}\zeta_0 \tan\varphi & c_{1\eta} = G_{13}\zeta_0 \tan\varphi \\
a_{1\zeta} = G_{11}(\xi_0 - \eta_0)\tan\varphi & b_{1\zeta} = G_{12}(\xi_0 - \eta_0)\tan\varphi & c_{1\zeta} = G_{13}(\xi_0 - \eta_0)\tan\varphi
\end{array} \tag{A1-2}$$

$$G_{11} = \left. \frac{a_1\eta + b_1}{(a_1 c_1 - b_1^2)\, r(\eta)} \right|_{\eta_1}^{\eta_2} \tag{A1-3}$$

$$G_{12} = -\left. \frac{b_1\eta + c_1}{(a_1 c_1 - b_1^2)\, r(\eta)} \right|_{\eta_1}^{\eta_2} \tag{A1-4}$$

$$G_{13} = \left. \frac{(2b_1^2 - a_1 c_1)\eta + b_1 c_1}{(a_1 c_1 - b_1^2)\, a_1\, r(\eta)} + \frac{1}{\sqrt{a_1^3}} \ln(\sqrt{a_1}\, r(\eta) + a_1\eta + b_1) \right|_{\eta_1}^{\eta_2} \tag{A1-5}$$

The coefficients $a_1, b_1, c_1,$ and $r(\eta)$ are:

$$r(\eta) = \sqrt{\eta^2 a_1 + 2\eta b_1 + c_1}$$

$$a_1 = 1 + \tan^2 \varphi$$

$$b_1 = -(\eta_0 + \xi_0 \tan\varphi)$$

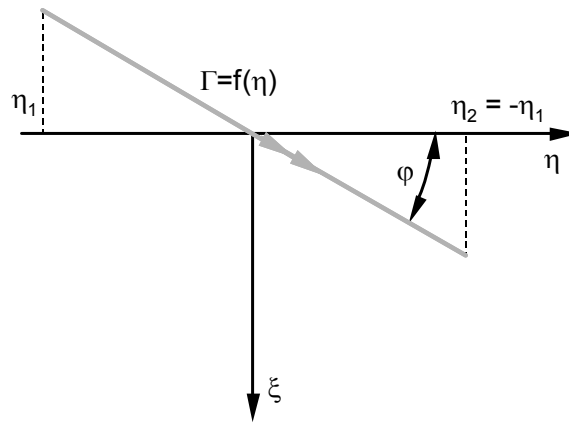$$c_1 = \xi_0^2 + \eta_0^2 + \zeta_0^2$$

(A1-6)

Figure A1-1: Local reference frame of a vortex filament.

Appendix 2: Induced Velocities of a Semi-Infinite Vortex Sheet with a Linear Vorticity Distribution

The integral in Eq. 6 yields the velocity at a point that is induced by a semi-infinite vortex sheet having a linear varying vorticity distribution in spanwise direction, $\gamma = B + 2\eta C$. As described in Ref. 28, the analytical integration can be written in the following way:

$$\underline{w}_2(\xi_0, \eta_0, \zeta_0) = \frac{1}{4\pi} \begin{bmatrix} 0 \\ Bb_{2\eta} + Cc_{2\eta} \\ Bb_{2\zeta} + Cc_{2\zeta} \end{bmatrix} \tag{A2-1}$$

Point $P_0(\xi_0, \eta_0, \zeta_0)$ is expressed with respect to the local reference frame of the semi-infinite vortex sheet as indicated in FigA2-1.

In accordance with in Ref. 28, the coefficients in Eq. A2-1 are computed using the following relationships:

$$b_{2\eta} = -\zeta_0 \sum_{\substack{i=1,2,6 \\ j=4,1,5}} G_{2i} b_{2j} \quad c_{2\eta} = -\zeta_0 \sum_{\substack{i=1,2,4,5,6 \\ j=4,1,3,7,5}} G_{2i} c_{2j}$$

$$b_{2\zeta} = \sum_{i=1}^{7} G_{2i} b_{2i} \qquad c_{2\zeta} = \sum_{i=1}^{7} G_{2i} c_{2i} \tag{A2-2}$$

The remaining relationships are also according to Ref. 28. The only extension is the positive constant k in Eqs. A2-5 and A2-9, which is part of the treatment of the singularities along the side edges of the semi-infinite vortex sheet as discussed in Chapter 3.1:

$$G_{21} = \left[\frac{\beta_1}{2\rho} \ln\mu_1(t) + \frac{\beta_2}{\rho} \mu_2(t) \right]_{t_1}^{t_2} \tag{A2-3}$$

$$G_{22} = \frac{1}{\xi_0}\left[-\frac{\beta_2}{2\rho}\ln\mu_1(t) + \frac{\beta_1}{\rho}\mu_2(t) \right]_{t_1}^{t_2}$$

(A2-4)

with

$$
\left.
\begin{aligned}
&\beta_1 = -\sqrt{\frac{\rho+\epsilon}{2}} \quad\quad \rho = \beta_1^2 + \beta_2^2 = \sqrt{\epsilon^2 + 4\zeta_0^2 b_2^2} \\
&\beta_2 = -\sqrt{\frac{\rho-\epsilon}{2}} \quad\quad \epsilon = (\xi_0 - \eta_0\tan\varphi)^2 - \zeta_0^2\tan^2\varphi \\
&\mu_1 = \frac{(\gamma_1 t + \delta_1 - r(t))^2 + (\gamma_2 t + \delta_2)^2}{k + t^2 + \zeta_0^2} \\
&\mu_2 = \arctan\frac{\zeta_0}{t} + \arctan\frac{\gamma_2 t + \delta_2}{\gamma_1 t + \delta_1 - r(t)} \\
&\gamma_1 = \frac{1}{\rho}(a_2\beta_2\zeta_0 + b_2\beta_1) \quad\quad \gamma_2 = \frac{1}{\rho}(a_2\beta_1\zeta_0 - b_2\beta_2) \\
&\delta_1 = \frac{1}{\rho}(b_2\beta_2\zeta_0 + c_2\beta_1) \quad\quad \delta_2 = \frac{1}{\rho}(b_2\beta_1\zeta_0 - c_2\beta_2)
\end{aligned}
\right\}
$$

(A2-5)

and

$$G_{23} = \left[\frac{1}{a_2}r(t) - \frac{b_2}{\sqrt{a_2^3}}\ln\mu_3 \right]_{t_1}^{t_2}$$

(A2-6)

$$G_{24} = \left[\frac{1}{\sqrt{a_2}}\ln\mu_3 \right]_{t_1}^{t_2}$$

(A2-7)

with

$$\mu_3 = a_2 t + b_2 + \sqrt{a_2}\,r(t)$$

A(2-8)

as well as

$$G_{25} = \left[\frac{1}{2}\ln(k + t^2 + \zeta_0^2) \right]_{t_1}^{t_2}$$

(A2-9)

where k is a positive constant. The special case k=0 is the original solution that is introduced in Ref. 28. Furthermore:

$$G_{26} = \left[\frac{1}{\zeta_0}\arctan\frac{t}{\zeta_0} \right]_{t_1}^{t_2}$$

(A2-10)

$$G_{27} = t_2 - t_1 \qquad \text{(A2-11)}$$

The coefficients a_2, b_2, c_2, and the variable $r(t)$ are:

$$r(t) = \sqrt{t^2 a_2 + 2tb_2 + c_2}$$
$$a_2 = 1 + \tan^2\varphi$$
$$b_2 = (\xi_0 - \eta_0 \tan\varphi)\tan\varphi \qquad \text{(A2-12)}$$
$$c_2 = (\xi_0 - \eta_0 \tan\varphi)^2 + \zeta_0^2$$
$$t = \eta_0 - \eta$$

The remaining variables of Eq. A2-2 are defined in the following way:

$$
\begin{aligned}
b_{21} &= -(\xi_0 - \eta_0 \tan\varphi) & c_{21} &= -2(\zeta_0^2 \tan\varphi + \eta_0(\xi_0 - \eta_0 \tan\varphi)) \\
b_{22} &= \zeta_0^2 \tan\varphi & c_{22} &= -2\zeta_0^2(\xi_0 - 2\eta_0 \tan\varphi) \\
b_{23} &= 0 & c_{23} &= 2\tan\varphi \\
b_{24} &= -\tan\varphi & c_{24} &= 2(\xi_0 - 2\eta_0 \tan\varphi) \\
b_{25} &= -1 & c_{25} &= -2\eta_0 \\
b_{26} &= 0 & c_{26} &= -2\zeta_0^2 \\
b_{27} &= 0 & c_{27} &= 2
\end{aligned}
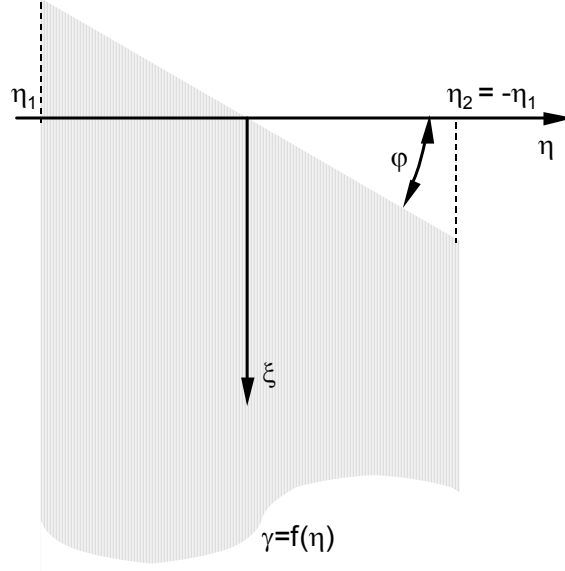\qquad \text{(A2-13)}
$$

Figure A2-1: Local reference frame of a semi-infinite vortex sheet.

Appendix 3: Induced Velocities of a Distributed Vorticity Element

The influence that a distributed vorticity element with index j has at a particular location $P(\xi,\eta,\zeta)$ is the compounded induction of two vortex filaments and two semi-infinite vortex sheets, as indicated in Fig. 11. Point P is expressed in the local reference frame of the distributed vorticity element as depicted in Fig. 10. The same figure shows the general relations and characteristics of the distributed vorticity element. The transformations between the local and global reference frames are listed in Eqs. 9 and 10. The subsequent induced velocity is:

$$\underline{w}_{3j}(\xi,\eta,\zeta) = \underline{w}_1(\xi-\xi_j,\eta,\zeta,A_j,B_j,C_j,\varphi_{j_{l.e.}}) + \underline{w}_1(\xi+\xi_j,\eta,\zeta,-A_j,-B_j,-C_j,\varphi_{j_{t.e.}})$$
$$+ \qquad\qquad\qquad\qquad (A3\text{-}1)$$
$$\underline{w}_2(\xi-\xi_j,\eta,\zeta,B_j,C_j,\varphi_{j_{l.e.}}) + \underline{w}_2(\xi+\xi_j,\eta,\zeta,-B_j,-C_j,\varphi_{j_{t.e.}})$$

The velocities that the vortex filaments, $\underline{w}_1$, and the semi-infinite vortex sheets, $\underline{w}_2$, induce, can be computed with the methods listed in Appendices 1 and 2, respectively. The computed velocities are expressed with respect to the local reference frame of the distributed vorticity element. The transformation into the global coordinate system is similar to the one in Eq. 10:

$$\underline{w}_{3j}(x,y,z) = \begin{bmatrix} \cos\psi_j\cos\varepsilon_j & -\sin\psi_j\cos\varepsilon_j & \sin\varepsilon_j \\[2ex] \cos\psi_j\sin\varepsilon_j\sin\nu_j & -\sin\psi_j\sin\varepsilon_j\sin\nu_j & \\ +\sin\psi_j\cos\nu_j & +\cos\psi_j\cos\nu_j & -\cos\varepsilon_j\sin\nu_j \\[2ex] -\cos\psi_j\sin\varepsilon_j\cos\nu_j & \sin\psi_j\sin\varepsilon_j\cos\nu_j & \\ +\sin\psi_j\sin\nu_j & +\cos\psi_j\sin\nu_j & \cos\varepsilon_j\cos\nu_j \end{bmatrix} \underline{w}_{3j}(\xi,\eta,\zeta) \quad (A3\text{-}2)$$

Under steady conditions, the vorticity remains constant in the streamwise direction. Thus, the influence of a vortex filament that, for example, is located along the leading edge of a distributed element is canceled by the influence of the filament along the trailing edge of the element that is directly upstream. Similarly, the influence of the vortex filament along the trailing edge is canceled by the leading edge vortex filament of the next distributed vorticity element downstream. Consequently, the first two terms on the right-hand side of Eq. A3-1, are disregarded in the wake, simplifying the velocity computation.

Appendix 4: Determining the Bound Circulation

In order to determine the circulation coefficients, A, B, and C, of distributed vorticity elements of a lifting surface, three boundary conditions are needed. The first one is the kinematic flow condition that requires the flow to be tangential to the surface at the control points of the bound distributed vorticity elements:

$$\underline{V}_\infty \cdot \underline{n}_i + \underline{w}_i \cdot \underline{n}_i = 0 \qquad \text{(A4-1)}$$

The index i denotes the control point at which the kinematic flow condition is satisfied. $\underline{n}_i$ is the local surface normal and $\underline{V}_\infty$ the velocity of the free stream. The velocity, $\underline{w}_i$, that is induced at control point i consists of two components: one that is induced by the distributed vorticity elements of the lifting surface, $\underline{w}_{i\,surface}$, and one that is induced by the distributed vorticity elements of the wake, $\underline{w}_{i\,wake}$. Since the latter induced velocity depends on the vorticity that has been shed into the wake during the previous time step, Eq. A4-1 can be separated into known and unknown velocity components:

$$\underline{w}_{isurface} \cdot \underline{n}_i = -\underline{V}_\infty \cdot \underline{n}_i - \underline{w}_{iwake} \cdot \underline{n}_i \qquad \text{(A4-2)}$$

The velocity induced by the wake at the control point i is, $\underline{w}_{i\,wake}$, is:

$$\underline{w}_{iwake}(x_0, y_0, z_0)_i = \sum_{j}^{n_{wake}} \underline{w}_{3j}(x_0, y_0, z_0)_i \qquad \text{(A4-3)}$$

where $\underline{w}_{3j}$ is the velocity component that the j-th wake element induces at the i-th control point. The wake consists of n_{wake} distributed vorticity elements. Each velocity component, $\underline{w}_{3j}$, is computed as described in Appendix 3 using the wake vorticity distribution of the previous time step. The velocities induced by the

$n_{surface}$ distributed vorticity elements of the lifting surface at the control point i remain unknown for now:

$$\underline{w}_{isurface}(x_0,y_0,z_0)_i = \sum_{j}^{n_{surface}} \underline{w}_{3j}(x_0,y_0,z_0)_i \qquad (A4\text{-}4)$$

The velocity that the j-th surface element induces at the i-th control point is:

$$\underline{w}_{3j}(\xi_0,\eta_0,\zeta_0)_i = \frac{1}{4\pi}\begin{bmatrix} A_j a_{3\xi ji} + B_j b_{3\xi ji} + C_j c_{3\xi ji} \\ A_j a_{3\eta ji} + B_j b_{3\eta ji} + C_j c_{3\eta ji} \\ A_j a_{3\zeta ji} + B_j b_{3\zeta ji} + C_j c_{3\zeta ji} \end{bmatrix} \qquad (A4\text{-}5)$$

This velocity can be transformed from the local reference frame of the j-th element to the global frame using Eq. A3-2. Similar to the description in Appendix 3, the influence coefficients, a_3, b_3, and c_3, are the compounded result of two vortex filaments and two semi-infinite vortex sheets. Thus, Eq. A4-5 can be rewritten as:

$$\underline{w}_{3j}(\xi_0,\eta_0,\zeta_0)_i = \frac{1}{4\pi}\begin{bmatrix} a_{1\xi l.e.ji} - a_{1\xi t.e.ji} & \begin{matrix} b_{1\xi l.e.ji} - b_{1\xi t.e.ji} \\ + b_{2\xi l.e.ji} - b_{2\xi t.e.ji} \end{matrix} & \begin{matrix} c_{1\xi l.e.ji} - c_{1\xi t.e.ji} \\ + c_{2\xi l.e.ji} - c_{2\xi t.e.ji} \end{matrix} \\ a_{1\eta l.e.ji} - a_{1\eta t.e.ji} & \begin{matrix} b_{1\eta l.e.ji} - b_{1\eta t.e.ji} \\ + b_{2\eta l.e.ji} - b_{2\eta t.e.ji} \end{matrix} & \begin{matrix} c_{1\eta l.e.ji} - c_{1\eta t.e.ji} \\ + c_{2\eta l.e.ji} - c_{2\eta t.e.ji} \end{matrix} \\ a_{1\zeta l.e.ji} - a_{1\zeta t.e.ji} & \begin{matrix} b_{1\zeta l.e.ji} - b_{1\zeta t.e.ji} \\ + b_{2\zeta l.e.ji} - b_{2\zeta t.e.ji} \end{matrix} & \begin{matrix} c_{1\zeta l.e.ji} - c_{1\zeta t.e.ji} \\ + c_{2\zeta l.e.ji} - c_{2\zeta t.e.ji} \end{matrix} \end{bmatrix}\begin{bmatrix} A_j \\ B_j \\ C_j \end{bmatrix} \qquad (A4\text{-}6)$$

The influence coefficients in Eq. A4-6, a_3, b_3, and c_3, can be transformed to the global reference frame with Eq. A3-2.

Ultimately, Eq. A4-2 leads to $n_{surface}$ linear equations when combined with

Eqs. A4-3 and A4-4. Further boundary conditions are required, however, in order

to solve for the $3n_{surface}$ unknown circulation coefficients of the distributed vorticity

elements of the lifting surface. In a manner similar to that of the multiple lifting

line method of Ref. 28 and as shown in Fig. 5, the spanwise continuity of the

bound circulation and of the vorticity provides the additional $2n_{surface}$ equations. If

indices i and i+1 denote the properties of two neighboring distributed vorticity

element of the lifting surface, their circulations and vorticities are equal at their

joined border:

$$A_i + \eta_i B_i + \eta_i^2 C_i - A_{i+1} + \eta_{i+1} B_{i+1} - \eta_{i+1}^2 C_{i+1} = 0 \qquad (A4\text{-}7)$$

$$B_i + 2\eta_i C_i - B_{i+1} + 2\eta_{i+1} C_{i+1} = 0 \qquad (A4\text{-}8)$$

The circulation of a distributed vorticity element that is located at the

wingtip becomes zero, thus:

$$A_{tip} + \eta_{tip} B_{tip} + \eta_{tip}^2 C_{tip} = 0 \qquad (A4\text{-}9)$$

Equations A4-2 through A4-9 can be formulated in matrix form:

$$[E] \cdot \{x\} = \{R\} \qquad (A4\text{-}10)$$

The influence matrix $[E]$ depends solely on the wing geometry and has $3n_{surface}$ x

$3n_{surface}$ elements. The vector $\{x\}$ consists of the unknown circulation coefficients

of the lifting surface elements, A, B, and C. One third of the elements of the

resultant vector $\{R\}$ depend on the scalar products of the local surface normal

and the sum of the free-stream and wake induced velocities. The remaining

$2n_{surface}$ elements are zero.

The system of $3n_{surface}$ equations can be solved for the vector $\{x\}$ using either a Gaussian algorithm or a lower-upper decomposition. The latter method reduces the number of computational steps, especially for a time-stepping application.

Vita

Götz Bramesfeld graduated as a Diplom Ingenieur from the Technical University of Braunschweig, Germany, in 1998. In 1999 he received a Master of Science in Aerospace Engineering from The Pennsylvania State University. After working for a year for the Piasecki Aircraft Corporation in Essington, Pennsylvania, he returned to Penn State completing his doctorate degree in Aerospace Engineering. While doing so, he was an instructor in the Department of Aerospace Engineering.